Polypharmacology of an Optimal Kinase Library

Caitlin E. Mills[1,2,*], Clemens Hug[1,*], Karuna Anna Sajeevan[3], Nicholas Clark[1,4], Chiara Victor[1,5], Mirra Chung[1], Sameer Rawat[9], Bree Aldridge[1,6,7], Mark W. Albers[1,8], Ratul Chowdhury[1,3], Benjamin M. Gyori[1,9,10], Peter K. Sorger[1,2,11,†]

*Authors contributed equally
[†]Corresponding Author: Peter K. Sorger; peter_sorger@hms.harvard.edu

[1]Laboratory of Systems Pharmacology, Harvard Program in Therapeutic Science, Harvard Medical School, Boston, MA, 02115, USA

[2]Department of Systems Biology, Harvard Medical School, 200 Longwood Avenue, Boston, MA 02115, USA

[3]Department of Chemical and Biological Engineering, Iowa State University, Ames, IA 50011, USA

[4]Current address: Department of Host-Microbe Interactions, St. Jude Children's Research Hospital, Memphis, TN, USA

[5]Current address: Lyell Immunopharma, Inc., Seattle, WA, USA

[6]Department of Molecular Biology and Microbiology, Tufts University School of Medicine and Stuart B. Levy Center for Integrated Management of Antimicrobial Resistance, Boston, MA, USA

[7]Department of Biomedical Engineering, Tufts University School of Engineering, Medford, MA, USA

[8]Department of Neurology, Massachusetts General Hospital, Charlestown, MA, USA

[9]Khoury College of Computer Sciences, Northeastern University, Boston, MA, USA

[10]Department of Bioengineering, Northeastern University, Boston, MA, USA

[11]Ludwig Centre at Harvard, Harvard Medical School, Boston, MA, 02115, USA

ORCID IDs:
Caitlin E. Mills - 0000-0002-2608-4084
Clemens Hug - 0000-0002-8299-3274
Karuna Anna Sajeevan - 0000-0002-9093-3845
Nicholas Clark - 0000-0003-0105-9605
Chiara Victor - 0000-0002-9002-1328
Mirra Chung - 0000-0002-4033-7930
Sameer Rawat - 0009-0006-9618-2153
Bree Aldridge - 0000-0003-2236-1424
Mark W. Albers - 0000-0001-7855-3455
Benjamin M. Gyori - 0000-0001-9439-5346
Ratul Chowdhury - 0000-0003-4522-6911
Peter K. Sorger - 0000-0002-3364-1838

ABSTRACT

Despite decades of research, current understanding of the spectrum of targets bound by kinase inhibitors remains incomplete. This complicates mechanism of action studies, drug repurposing, and understanding of adverse responses. Here, we describe kinome-wide profiling of an optimal kinase library (OKL) comprising 192 small molecules selected based on stage of clinical development, chemical diversity, and target coverage. Our results show that polypharmacology is widespread among kinase inhibitors independent of regulatory approval. The generally understood ("assigned") targets of approved molecules are not necessarily the most potently inhibited and off targets include multiple understudied kinases. Moreover, median selectivity has not increased over time. We illustrate the use of synoptic OKL-kinome profiles in identifying potential toxicity targets, repurposing anti-inflammatory drugs for neurodegenerative and infectious diseases, and performing chemical genetic studies. Our studies illustrate how much remains to be discovered about the chemistry and biology of one of the largest classes of human therapeutics.

INTRODUCTION

Optimizing the selective binding of a chemical compound to a desired protein target is a key step in small molecule drug development. This is particularly true in the case of targets that are members of multi-protein families. The human kinome comprises ~530 proteins (with the number somewhat dependent on definition)[1] and as of 2026, over 100 kinase inhibitors have been FDA approved for use as therapeutics[2] with an additional 369 compounds against 129 targets undergoing clinical trials[3,4]. This represents one of the most active areas of drug discovery: there were more kinase inhibitors approved by the FDA in 2025 than in any prior year[5]. In current practice, kinase inhibitors are most commonly designed to bind one or a small set of closely related members of the kinome (we refer to these as "assigned" targets). It is therefore common to describe drug '*A*' as an inhibitor of assigned target '*B*', but it is generally understood that binding to other targets (polypharmacology) plays an essential – if poorly understood – role in drug activity. Kinase inhibitors achieve regulatory approval based on clinical endpoints, survival in the case of anti-cancer drugs, but a description of their mechanism of action is an essential component of regulatory filings, and this invariably emphasizes the presumed role of assigned target(s). A complete understanding of how inhibition of other potential targets contributes to the clinical success of small molecules often occurs post-approval and is broadly dependent on better ways of assessing polypharmacology.

Both academic and commercial platforms exist to profile the binding affinities of small molecules against the great majority (~75%) of all protein kinases. Several high-impact projects have studied the polypharmacology of kinase inhibitors at scale[6–10] using compound libraries that vary in composition. Despite a steady stream of drug approvals, it has been some time since kinase inhibitor

polypharmacology has been studied in depth. This paper also exploits cheminformatics tools able to assemble libraries that strike a balance between chemical diversity, selectivity, stage of clinical development, and library size (and thus, cost). The resulting 192 compound Optimal Kinase Library (OKL) is one example of a library optimized on several competing characteristics.

The literature on protein kinase inhibitors is large, and affinity data obtained from the literature are actively curated in public databases such as ChEMBL[11], IDG Pharos[12] and BindingDB[13]. Metrics such as affinity spectra (TAS)[14] consolidate available data on inhibitor binding and non-binding relationships in public data while accounting for uncertainty in the underlying evidence. However, systematic analysis of polypharmacology is not as simple as assembling literature knowledge. For kinase inhibitors, this literature relies on a wide range of assay types (e.g. enzymatic inhibition, affinity mass spectrometry, binding to recombinant protein libraries) and conditions (e.g. ATP or substrate concentration) with few overlapping data points. This makes kinome-wide analysis difficult. Moreover, affinity screening is often biased toward assigned target(s), suspected off-targets, and “toxicity” targets known to limit clinical utility. Data on “known non-binders” is particularly sparse, even though it is essential for establishing selectivity[14]. Thus, existing knowledge is too incomplete to answer basic questions about the breadth and significance of compound polypharmacology.

In this paper we use the OKL and Eurofins’ KINOMEscan platform[15] to collect kinome-wide affinity data at four concentrations for 192 kinase inhibitors optimized for selectivity, affinity, and approval status. We introduce a Bayesian inference framework to estimate Kds for all inhibitor-kinase pairs, enabling inference of affinities outside tested concentrations. We find that OKL compounds have various degrees of polypharmacology and inhibit all assayed kinases (including pathogenic kinases from tuberculosis and malaria). Kinase clustering based on OKL inhibitor binding data differs from the familiar view of the kinome tree based on sequence similarity, demonstrating that sequence alignment is an imperfect way of thinking about polypharmacology. We illustrate the utility of the fully annotated OKL as a screening tool by using it to dissect, identify and characterize neuroprotective agents active in a model of Alzheimer’s disease, investigate vulnerabilities in a model of cisplatin-resistant ovarian cancer, and identify inhibitors of non-mammalian pathogenic kinases. These use cases show that systematic kinome-scale knowledge of kinase polypharmacology has broad utility across biological contexts.

RESULTS

Establishment of kinome-wide affinities for a practically scaled Optimal Kinase Library

The larger and more diverse a chemical library and the more comprehensive the data on activity the greater the insight into compound-target relationships. However, collecting kinome-wide affinity data is expensive; for 10-point enzymatic assays this is ~$100/curve or $10M for 200 compounds against

500 targets. The KINOMEscan® kinome-scale profiling assay available from Eurofins is 5-10-fold cheaper and has therefore been used in more than 2,000 publications. Systematic profiling is nonetheless sufficiently expensive to require compact libraries[6–9,14,16–18]. Thus, the OKL in this work aimed for a minimal collection balancing target coverage and structural diversity so that, ideally, each kinase was bound by two inhibitors with the highest possible selectivity and the greatest difference in chemical structure (i.e. Tanimoto similarity <= 0.2 between pairs based on Morgan fingerprints with 2 Å radius)[14]. When a choice was available, we selected compounds that were approved for use in humans. This resulted in a 192-compound library comprising 44 FDA-approved drugs, 98 molecules that have been, or are currently, in clinical trials, and 50 pre-clinical "tool" compounds having a total of 115 unique assigned targets (**Figure 1a-b).** Overlap between libraries previously subjected to systematic kinome profiling and OKL was surprisingly limited (**Figure 1c**) due to differences in study goals, our emphasis on target and chemical diversity, and a steady increase in the scope of clinical approvals[6–9,17]. For this reason, and those outlined above, knowledge of kinome-wide binding by OKL inhibitors was sparse (**Figure 1d**).

KINOMEscan scanMAX profiling (hereafter KINOMEscan) is based on a competitive binding assay comprising 406 wildtype (WT) human kinases and 59 kinases carrying oncogenic or resistance mutations[19,20] plus three non-mammalian kinases (the availability of kinases is dependent in part on the feasibility of making them recombinantly). In KINOMEscan, a compound of interest is incubated with oligo-tagged recombinant kinases and immobilized ATP-like ligands capable of binding all kinases in the library; the amount of ligand-bound kinase is measured by qPCR to generate a 'percent of control' value (relative to incubation with DMSO); a value of 0 denotes strong binding and 100 no binding. We assayed each OKL inhibitor at four concentrations spanning four orders of magnitude (10 μM, 1 μM, 100 nM and 12.5 nM) to generate 89,856 four-point dose response curves (192 OKL compounds x 468 targets). Quality control (see Methods, **Supplementary Figure 1**) revealed ~900 *discordant* dose response profiles (~1% of the data) in which percent control did not fall with increasing inhibitor concentration (**Supplementary Figure 1**). These data were omitted from further analysis.

We explored a variety of approaches for estimating KINOMEscan-derived dissociation constants (^{KS}Kd) and settled on Bayesian inference. Bayesian modeling substantially improved the reliability of (^{KS}Kd) estimations compared to linear interpolation, particularly when values were below the lowest concentration tested experimentally (12.5 nM; see **Supplementary Note**) and resulted in a more complete view of kinome-wide binding for OKL inhibitors (**Figure 1e**). Those inhibitor-kinase pairs for which data were available in ChEMBL exhibited good agreement (R = 0.91) with ^{KS}Kd estimates (**Figure 1f-g**). Two key features of a library of small molecule inhibitors are coverage – how many targets are bound by how many inhibitors; and selectivity – how many targets are preferentially (selectively) bound by any inhibitor. OKL achieve full coverage of all 468 assayed targets at a relatively high inhibitor concentration of 1 μM or below (2-130 inhibitors per kinase at ^{KS}Kd ≤ 1 μM) and 94%

coverage of WT kinases at 100 nM or below (0-57 inhibitors for 379/406 WT kinases at ^{KS}Kd ≤ 100 nM); at this lower concentration all mutant kinases were also inhibited, likely because they have been the focus of years of intensive medicinal chemistry (**Figure 2a-b, Supplementary Figure 2a-c**). Note that these estimates of kinome coverage are substantially greater than what can be inferred from Eurofins' standard recommendation that a binder is simply a molecule that achieves <35% of control activity at a single dose.

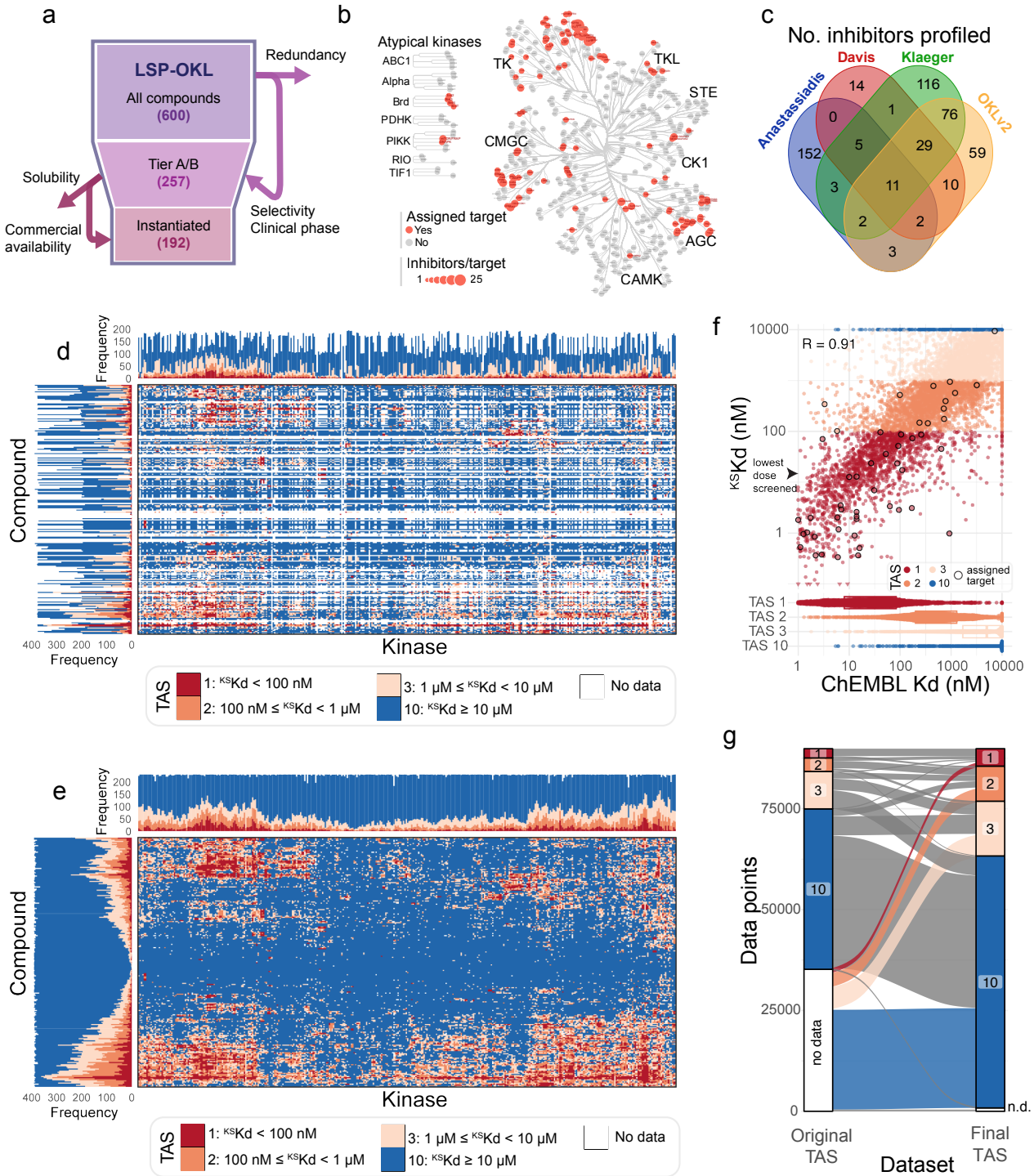

Figure 1: A complete view of kinome-wide affinities for the 192 compound 'Optimal Kinase Library'. (a) Schematic representation of the reduction of OKL from 600 compounds to the instantiated OKL set of 192 compounds. **(b)** The nominal targets of OKL compounds shown on the kinome tree; red indicates a nominal target and the size of the spot indicates the number of inhibitors per target. **(c)** Venn diagram showing the overlap between the inhibitors profiled in similar efforts and those in OKL. **(d)** Kinome-wide target affinity spectra based on ChEMBL data for all OKL compounds prior to the current study. **(e)** Kinome-wide target affinity spectra for all OKLv2 compounds after the addition of the data generated in the current study. **(f)** Scatterplot comparing the ^{KS}Kd values measured in this paper to those previously available in ChEMBL. Data points are colored by TAS value, and the values for each compound's assigned target(s) are outlined in black. **(g)** An alluvial plot depicting the knowledge gained from addition of the data generated in the current study. TAS values on the left are from (c) and on the right from (d).

Kinase inhibitor selectivity for tool compounds and human therapeutics

Several metrics are available for quantifying library selectivity;[6,21,22] we used the easily-understood partition index (PI), which represents the fraction of an inhibitor bound to each kinase (having a ^{KS}Kd estimate) in a theoretical situation in which all kinases are present in excess[21]. A perfectly selective inhibitor binding a single target would have a maximum PI (PI_{max}) = 1 and an inhibitor binding many targets with similar affinity would have $PI_{max} << 1$. As an example, PI_{max} values for OKL inhibitors spanned a range from < 0.1 for AMG-208 to > 0.98 (for tepotinib binding to the MET receptor tyrosine kinase; RTK) (**Figure 2c-e**). We identified 69 "highly selective" compounds that bound to 37 WT kinases with $PI_{max} > 0.5$, but maximum selectivity for most kinases was $PI_{max} < 0.2$ (**Figure 2f-g**). This suggests that they are only bound by compounds that inhibit other kinases at similar concentrations**.**

Using OKL-KINOMEscan data, we examined four prevailing assumptions about the development of kinase inhibitors as human therapeutics: (i) approved drugs are more selective than compounds that failed in clinical trials (where 'failed' is defined as a trial compound not approved and no longer under investigation[3]); (ii) assigned targets are generally potently and selectively inhibited, particularly for FDA-approved drugs; (iii) compound selectivity has increased over time; and (iv) understudied (dark) kinases (per the definition of the NIH Investigating the Druggable Genome project)[23] are less widely inhibited than well-characterized (illuminated) kinases.

First, we grouped compounds based on maximum reported clinical trial phase, approval status, or trials registered in ClinicalTrials.gov and found that FDA-approved drugs do not differ from compounds in other stages of clinical development in terms of coverage or selectivity; however, purely pre-clinical tool compounds are on average less selective (**Figure 2h-i, Supplementary Figure 2d-e**). Second, while most assigned targets are bound with high affinity (**Figure 2g**, ^{KS}Kd ≤ 10 nM for 48% of assigned targets), selectivity varied widely (PI = 0 to 0.98, median 0.06, mean 0.17; **Figure 2k**) suggesting that many compounds are potent but not highly selective. Considering only FDA-approved drugs, an assigned target was the *highest* affinity target in only 23% of cases examined; for compounds that are not FDA-approved the proportion was 37% (**Figure 2l**). Thus, if we define a promiscuous

inhibitor as one that that binds many kinases, and a promiscuous kinase as one that binds many inhibitors, profiling of the OKL library revealed a wide range of promiscuity in inhibitors and kinases, even among FDA-approved drugs. Moreover, if we use the year of first publication to estimate the "age" of an OKL compound we find that average selectivity has not changed significantly over time. Thus, high selectivity (PI_{max} value) has not been necessary for past clinical success with kinase inhibitors. However, the highest selectivity achieved by a single compound has increased (**Figure 2m;** dark dotted line) reflecting the presence of outliers in the data presumably arising from advances in kinase inhibitor medicinal chemistry.

Kinase anti-targets and dark kinases

The concept of an anti-target, a protein that must be spared during drug discovery, is exemplified by the cardiac K+ channel hERG[24]. It has been proposed that some kinases also represent anti-targets[25,26]. Although no definitive list of kinase anti-targets has as-yet been assembled, unwanted inhibitor interactions should be identifiable in OKL-KINOMEscan data. One striking and unreported example involves alectinib (approved as Alecensa® for metastatic non-small cell lung cancer) which has ALK as an assigned target. OKL-KINOMEscan suggests that alectinib can also bind PHKG2, the liver-specific γ-subunit of the phosphorylase kinase; using enzymatic assays we confirmed that alectinib is an IC50= 33 nM inhibitor of PHKG2 (**Supplementary Figure 2h**). Mutation in PHKG2 give rise to severe liver disease[27] and inhibition of the kinase by sunitinib causes liver toxicity[28]. Hepatotoxicity leading is a recognized problem in up to 60% of patients treated with alectinib[29] (with grade 2-4 toxicity in 5-8% of patients) and we speculate that this is a consequence of inhibition of PHKG2. Examination of ^{KS}Kd values for ALK inhibitors across the OKL-KINOMEscan dataset show that a subset also target PHKG2 but that others do not. It should therefore be possible to create potent ALK inhibitors in which PHKG2 is not bound, thereby reducing hepatoxicity.

Wide differences in the levels of attention given to kinases over time has given rise to the concept of "understudied" or dark kinases[30] (the focus of a major NIH program)[31]. We found that these understudied kinases[23] were widely bound and selectivity inhibited even by FDA-approved compounds (**Figure 2n, Supplementary Figure 2f, g**). The number of OKL compounds inhibiting dark kinases was less than for illuminated kinases however (median of 5 vs 8 inhibitors per kinase at a threshold of ^{KS}Kd ≤ 100 nM, respectively). These largely uncharacterized inhibitory activities represent a potential starting point for targeting understudied kinases and may also provide insight into efficacious off-target activities of existing human therapeutics.

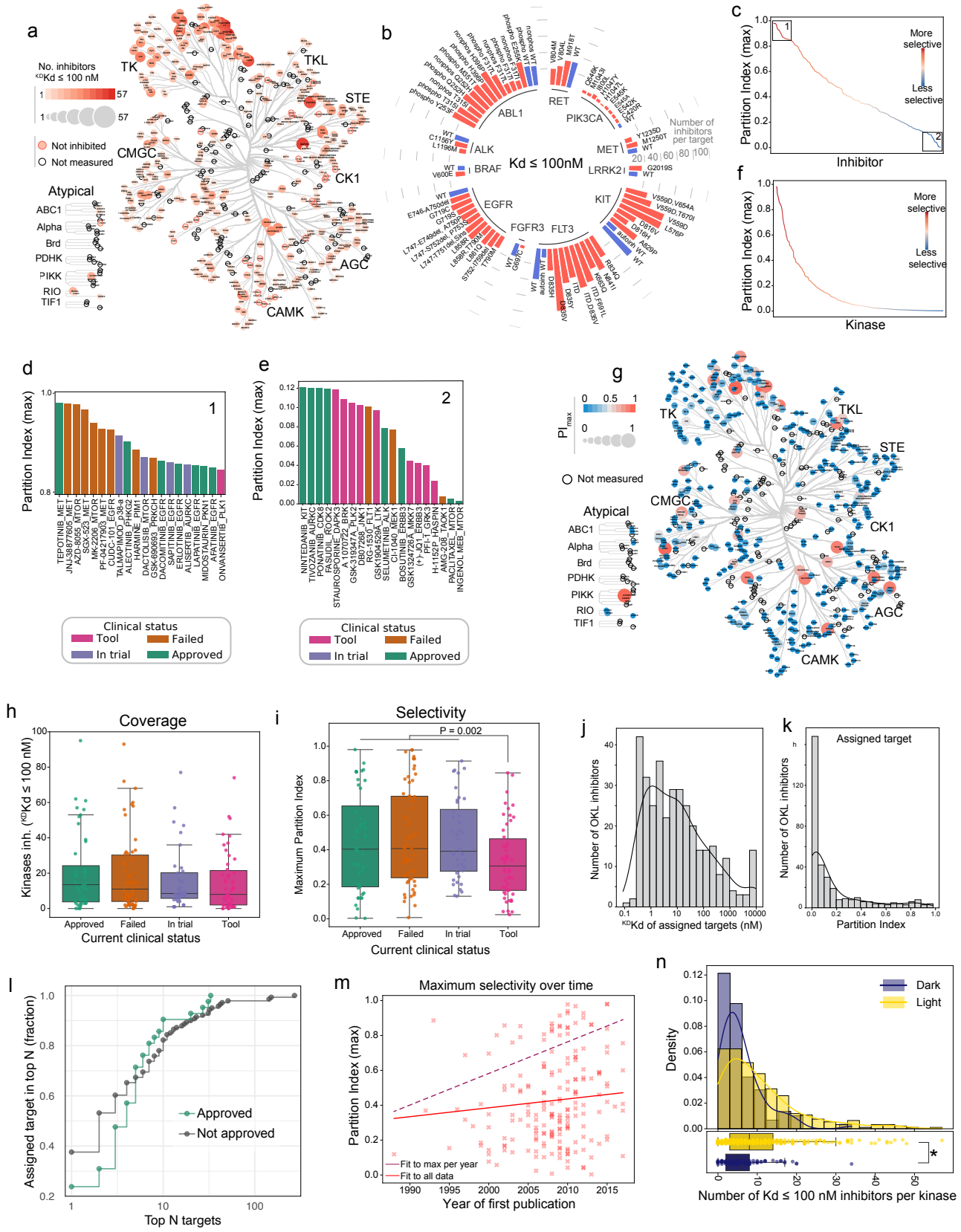
a
No. inhibitors
KDKd ≤ 100 nM
Not inhibited
Not measured
Atypical
ABC1
Alpha
Brd
PDHK
PIKK
RIO
TIF1
TK
TKL
STE
CMGC
CK1
AGC
CAMK
b
Kd ≤ 100nM
Number of inhibitors per target
ABL1
ALK
BRAF
EGFR
FGFR3
FLT3
KIT
LRRK2
MET
PIK3CA
RET
c
Partition Index (max)
Inhibitor
More selective
Less selective
d
Partition Index (max)
Clinical status
Tool
Failed
In trial
Approved
e
Partition Index (max)
Clinical status
Tool
Failed
In trial
Approved
f
Partition Index (max)
Kinase
More selective
Less selective
g
Not measured
Atypical
h
Coverage
Kinases inh. (KDKd ≤ 100 nM)
Approved
Failed
In trial
Tool
Current clinical status
i
Selectivity
P = 0.002
Maximum Partition Index
Approved
Failed
In trial
Tool
Current clinical status
j
Number of OKL inhibitors
KDKd of assigned targets (nM)
k
Assigned target
Number of OKL inhibitors
Partition Index
l
Assigned target in top N (fraction)
Approved
Not approved
Top N targets
m
Maximum selectivity over time
Partition Index (max)
Fit to max per year
Fit to all data
Year of first publication
n
Dark
Light
Density
Number of Kd ≤ 100 nM inhibitors per kinase

Figure 2: Kinome coverage and selectivity of OKL inhibitors. (a) The number of OKL inhibitors (^{KS}Kd < 100 nM) per kinase shown on the kinome tree by the size and intensity of the markers. Kinases not inhibited are outlined in red, kinases not assayed are outlined in black. **(b)** Radial bar plot showing the number of OKL inhibitors with ^{KS}Kd ≤ 100 nM for all mutant kinases (red bars) assayed in the KINOMEscan panel. WT kinases are indicated with blue bars. **(c)** The maximum partition index (PI_{max}) for each inhibitor in OKL. The inset barplots show the most (top) and least (bottom) selective inhibitors and associated kinase target colored by current clinical status. **(d)** PI_{max} for each kinase. The inset CORAL tree shows the PI_{max} for each kinase, the darker and redder the circle, the more selectively that kinase is inhibited by an OKL compound. **(e)** Boxplot showing the number of kinases per inhibitor with ^{KS}Kd ≤ 100 nM by clinical status. **(f)** Boxplot showing the maximum partition index for each OKL inhibitor by clinical status. P-value is from a Welch's t-test comparing tool compounds to all others. **(g)** Histogram of the ^{KS}Kd values for the assigned target(s) of OKL compounds. **(h)** Histogram of the partition indices for the assigned target(s) of OKL compounds. **(i)** Cumulative stairstep plot showing how often the nominal target is in the top N targets by ^{KS}Kd for approved (green) and not approved (gray) inhibitors. **(j)** Scatterplot showing PI_{max} with respect to the year each compound was first published. The lines of best fit to all data points and to the highest datapoint per year are shown in solid red and dashed maroon, respectively. **(k)** Histogram showing the number of OKL inhibitors that bind each dark and illuminated kinase with ^{KS}Kd ≤ 100 nM. Boxplots representing the same data are shown below the histograms. The * indicates Welch's t-test P < 0.0001.

Kinase promiscuity is associated with a DFG-out conformation binding Type I and II inhibitors

What is the basis of promiscuous binding of some human kinases to ATP-competitive inhibitors? To address this, we focused on the 18 most promiscuous kinases in our dataset (15 TKs, two STE kinases, and one CAM kinase; **Figure 3a**) each of which bound ≥ 33 compounds with relatively high affinity (^{KS}Kd ≤ 100 nM). Overlap among these inhibitors was limited with at most two inhibitors binding to 16/18 promiscuous kinases (**Figure 3b**, blue points); for example, MEK5 (**Figure 3b**, red point) was bound by five inhibitors that did not bind any other promiscuous kinases (at ^{KS}Kd ≤ 100 nM). Thus, promiscous kinases do not simply bind a common set of promiscuous inhibitors.

Identified structural determinants of binding specificity for ATP-competitive kinase inhibitors focus on the conformation and local environment of a conserved three amino acid motif (DFG) that lies immediately N-terminal to the activation loop[32]. Kinases assume both a *DFG-in* conformation, which is generally catalytically active, and a *DFG-out* conformation, which is inactive. Kinase inhibitors are classified into type I inhibitors that bind both DFG-in and DFG-out conformations and type II inhibitors that bind only DFG-out conformations; type III and IV inhibitors (so-called "allosteric inhibitors") bind outside the active site and are substantially less common[33]. We found that 14/18 promiscuous kinases were bound by more type II inhibitors than expected by chance (given OKL composition) (**Figure 3c**) consistent with binding to a DFG-out conformation. Moreover, kinases with a DFG-out structure in the Protein Data Bank (PDB)[34] were more promiscuous than those without (**Figure 3d,** mean number of ^{KD}Kd ≤ 100 nM inhibitors 15.5 and 8.3, respectively; Welch's t-test P = 2.66 x 10^{-5}). This difference was greatest for kinases in the STE and TK families (**Figure 3e**).

Six RTKs promiscuous for OKL compounds (PDGFRA, PDGFRB, KIT, CSF1R, DDR1, DDR2) were previously shown to bind many members of the 645-compound PKIS2 library, which has no overlap with OKL[35,16]. This was attributed to stabilization of the DFG-out conformation by a D671 to R752 salt bridge (the numbering is based on the DDR1 kinase)[35] (**Figure 3f**, red arrows). In our study, three additional RTKs (TRKA, TRKB and FLT3) having analogous D671 and R752 residues (**Figure 3f**, blue arrows) were also promiscuous. However, the same residue pair is present in four kinases that are not RTKs and are not promiscuous suggesting the impact of this feature on inhibitor binding is limited to RTKs. Thus, kinase promiscuity is associated with binding to the DFG-out conformation and for RTKs this is stabilized by a D671 to R752 salt bridge. Since several of these proteins are being targeted for development of human therapeutics, we asked whether promiscuity is incompatible with selective inhibition. Our data suggest that the answer is no: DDR1, for example, is bound by 41 OKL compounds (^{KS}Kd ≤ 100 nM) but one of these (Nilotinib, whose assigned target is BCR-ABL) is highly selective, with a partition index of 0.81 (**Figure 3g**, red point).

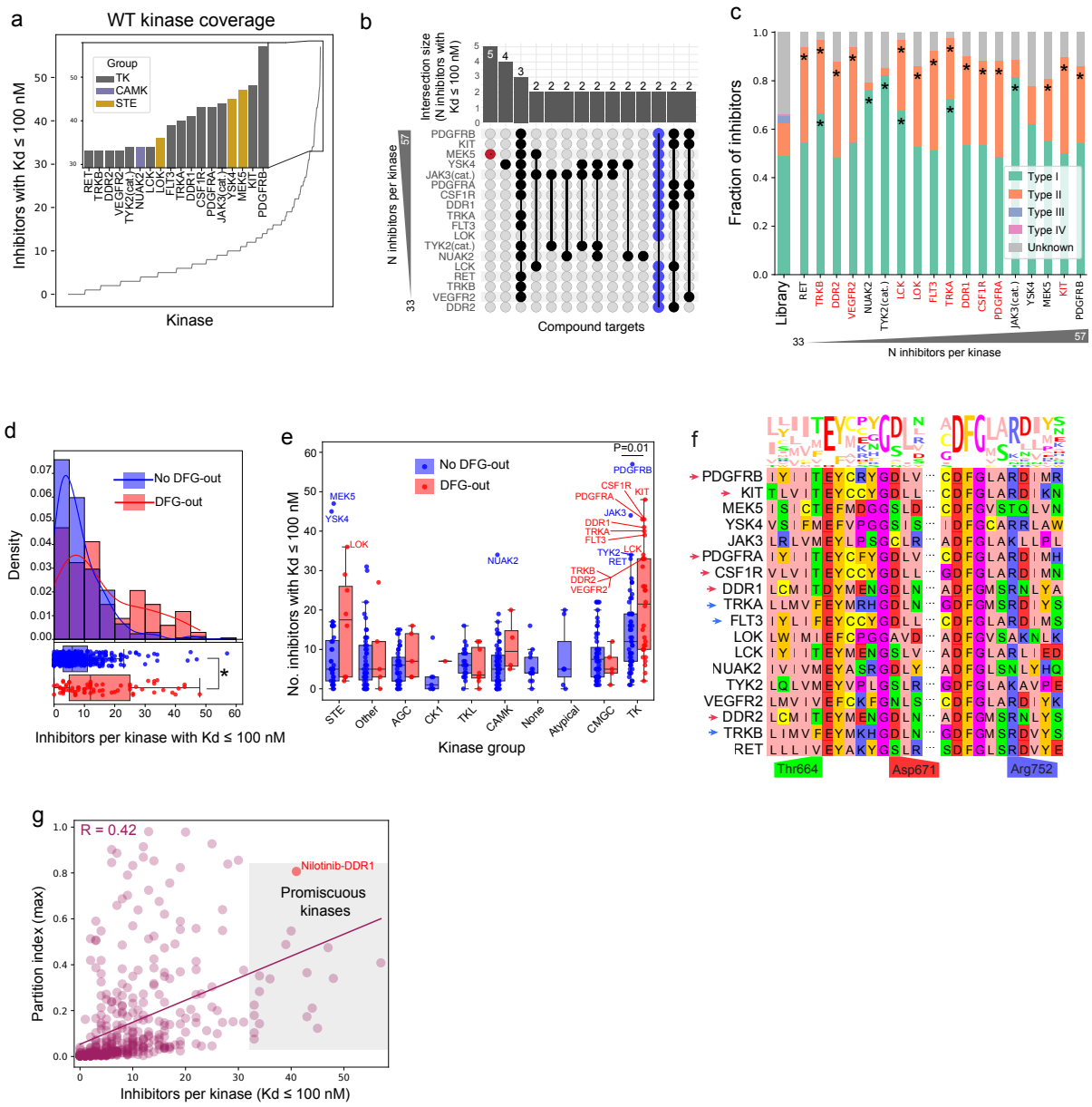

Figure 3: A subset of kinases are promiscuous for OKL inhibitors. (a) The number of OKL inhibitors (^{KS}Kd ≤ 100 nM) per kinase. The top 15 ranks with ties are shown in the inset bar plot colored by kinase group. These 18 kinases are referred to as promiscuous. **(b)** Upset plot showing the number of overlapping inhibitors with ^{KS}Kd ≤ 100 nM for the promiscuous kinases. **(c)** Stacked bar graph showing the distribution of inhibitor types in OKL and that bind each promiscuous kinase. Kinases identified as promiscuous in a previous study are in red. **(d)** Histograms of the number of inhibitors per kinase with ^{KS}Kd ≤ 100 nM for kinases with (red) and without (blue) reported DFG-out structures. KDE plots are overlaid for visualization. Boxplots representing the same data are shown below the histograms. The * indicates Welch's t-test P < 0.0001. **(e)** Boxplots of the number of inhibitors with ^{KS}Kd ≤ 100 nM for kinases with (red) and without (blue) DFG-out structured by kinase group. Welch's t-tests were performed on all pairs, P-values are only shown where P < 0.05. **(f)** Multiple sequence alignment and sequence logo plot of the promiscuous kinases. Residues previously implicated in RTK promiscuity are labeled. Amino acids are colored by the zappo color scheme. **(g)** Scatter plot of the number of inhibitors per kinase with ^{KS}Kd ≤ 100 nM with respect to the kinase's maximum partition index. Promiscuous kinases are in the shaded gray box.

Sequence homology and inhibitor binding provide distinct views of the kinome

The classic kinome tree is based on classification by Manning, et al.[36] in which kinases are clustered based on sequence homology (primarily in the catalytic domain). The tree is split into nine major groups (e.g. TKs, CAM kinases, AGC kinases, etc.) that each contain multiple families. Targeting specific isoforms within these families is a common goal of drug discovery, as exemplified by the search for PI3K inhibitors that discriminate between oncogenic kinases and immune regulators[37]. To see if OKL affinity data could assist in similar tasks, we performed hierarchical clustering based on the Spearman correlation of ^{KS}Kd values. This yielded nine major clusters (**Figure 4a, b**) that differed substantially from the groups generated from sequence similarity (**Figure 4b**). Taking the CMGC group as an example (**Figure 4b**, dotted outline), the 14 kinases in the MAPK family form one sequence-based cluster but six OKL clusters (**Figure 4b**, blue branch; **Figure 4c**). Thus, proteins most related in sequence can have very different inhibitor binding profiles: ERK1 and ERK2 are bound by different OKL inhibitors than ERK3 and ERK4, for example. In contrast, a second branch in the CMGC group comprising DYRK and SRPK family kinases lie in a single OKL cluster with a single outlier: HIPK4 (**Figure 4b**, red branch; **Figure 4d**). A HIPK4 inhibitor (**Figure 4e**) is more likely to bind other kinases in OKL cluster 3 which includes c-Jun N-terminal kinases (JNK1, JNK2, JNK3) which are in the MAPK family (**Figure 4a-d**). Inhibitor selectivity therefore represents a different way of viewing the kinome tree than sequence similarity and can be used to prioritize off-targets for deeper analysis. With additional data, it should be possible to extend this idea and construct a kinome tree based entirely on small molecule binding as opposed to sequence similarity.

The CDC2-like kinases (CLKs) have been linked to diseases ranging from cancer to neurodegeneration,[38] and CLK inhibitors are under investigation for multiple types of cancer. CLK1, CLK2, and CLK4 cluster tightly together based on OKL binding profiles but CLK3 - like HIPK4 - is an outlier relative to its closest homologues (**Figure 4f, g**). To investigate residues involved in small molecule binding by CLK3, we performed 500 ns all-atom molecular dynamics (MD) simulations for eight inhibitors having a range of affinities for CLK kinases. Starting the simulation with compounds outside the binding pocket, we found that high affinity CLK3 binders entered and remained in the pocket as measured by the distance from residue A319 on the pocket floor (< 0.4 nm for PF-3758309 and RG-547, and ~1.2 nm for THZ1; **Figure 4h**) and this corresponded to computational binding scores < -75 (**Figure 4i**). In contrast, inhibitors with ^{KD}Kd ≥ 1000 nM for CLK3 remained distant (~2.5 nm) from the pocket floor over the 500 ns simulation suggesting that they failed to enter the pocket, thereby reproducing the experimental data. Simulations suggested that two residues differing between CLK3 and other CLKs at the pocket entrance are likely involved in this selectivity: T166→N161, L246→K241 (number based on CLK3 residue positions; **Figure 4j**). These residue positions are known, along with V324→A319 on the pocket floor, to affect the charge distribution and size of the drug/ATP binding pocket.[39,40] Thus, subtle structural differences in kinase binding pockets that are not discernable by

sequence alignment can be detected by OKL kinome profiling and potentially used to guide isoform-selective inhibitor development.

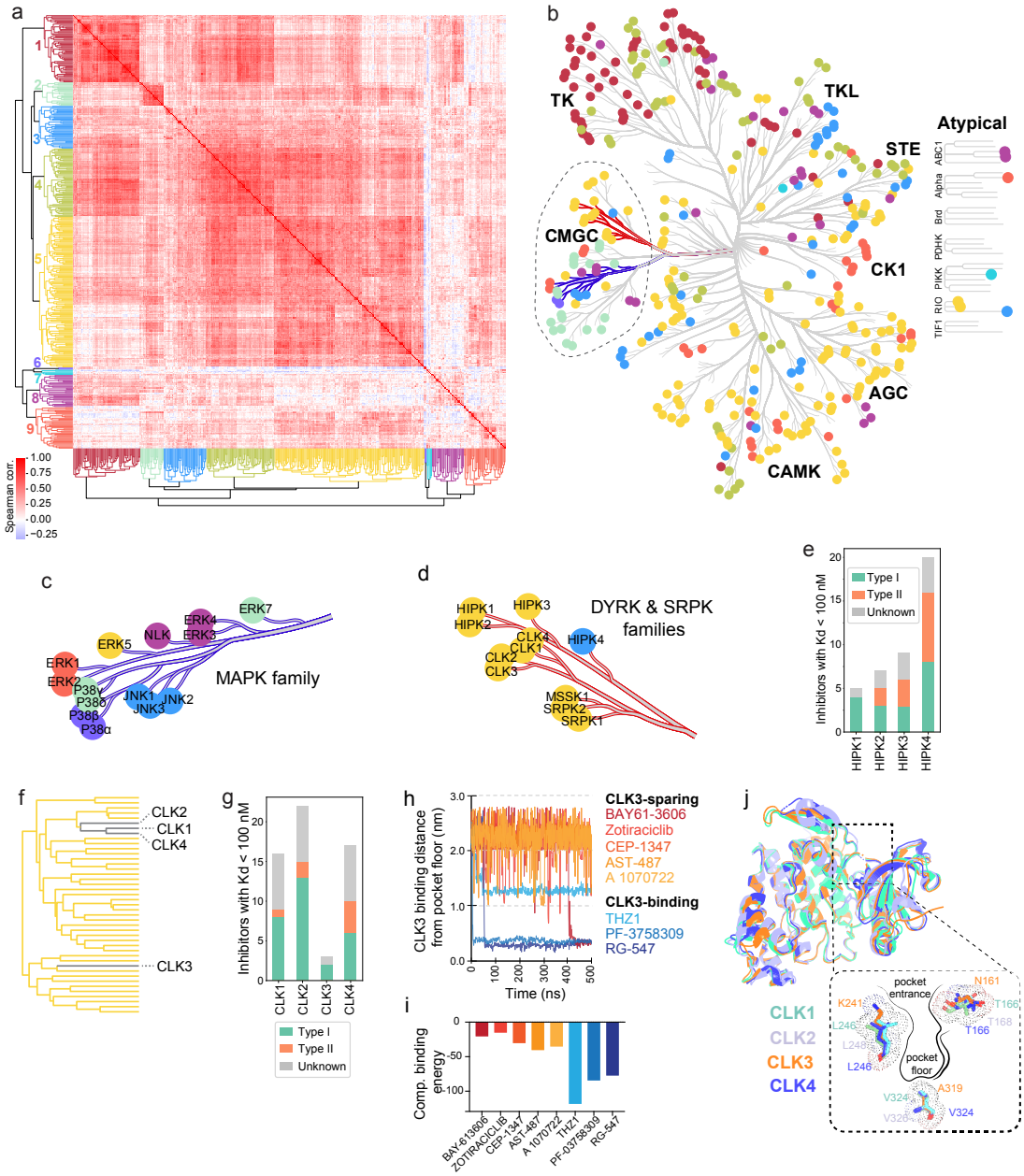

Figure 4: Kinase sequence homology with respect to OKLv2 compound affinities. (a) Hierarchical clustermap of the spearman correlation between kinases based on their ^{KS}Kd values for all OKL compounds. **(b)** The colors of the clusters are overlaid on the kinome tree. The blue branches are magnified in **(c)** and the red branches in **(d)**. **(e)** Bar plot of the number of OKL inhibitors with ^{KS}Kd ≤ 100 nM for each HIPK colored by inhibitor type. **(f)** Subset of the hierarchical tree from (a) showing the positions of each CLK. **(g)** Bar plot of the number of OKL inhibitors with ^{KS}Kd ≤ 100 nM for each CLK colored by inhibitor type. **(h)** 500ns molecular dynamics trajectories showing the distance of the indicated inhibitors from the floor of CLK3's binding pocket. **(i)** Computational binding energy scores from GROMACS molecular dynamics simulations of eight inhibitors with CLK3. **(j)** A visual overlay of the overall structures of CLK1,2,3, and 4 and zoomed-in view of their binding pockets highlighting key amino acids.

Using an optimized kinase library and affinity data to explore nuerodegeneration

To explore practical uses of OKL data, we performed cell-based screening in three distinct biological contexts: (i) rescue of neuronal cell death in a model of Alzheimer's disease (ii) identifying targets for killing of platinum resistant ovarian cancer cells and (iii) identification of inhibitors of non-mammalian kinases. A subset of AD is thought to involve neuronal death triggered by an inflammatory response to cytoplasmic double stranded RNA (cdsRNA).[41] This can be recapitulated in a cell-based screen by treating differentiated ReNVM neurons with the dsRNA mimetic, polyI:C, which leads to type I interferon signaling and cell death. Neuronal death can be rescued to variable degrees by Janus family kinase inhibitors (the JAK family comprises JAK1-3 and TYK2)[41,42] (**Figure 5a**). To determine if off targets were involved in rescue, we extended the OKL dataset by performing KINOMEscan profiling on 12 additional JAK inhibitors, focusing on the two most informative concentrations: 100 nM and 10 μM; the resulting OKL+JAKi dataset included a total of 21 inhibitors with assigned targets in the JAK family. We then screened the OKL at 1 μM in ReNVM cells treated with polyI:C and identified 14 inhibitors that conferred a significant (20% or greater) increase in viability (**Figure 5b**). In the subsequent rescreen, these 14 hits, and all compounds with one or more assigned targets in the JAK family (33 compounds in total), were then tested for rescue at four doses (10, 1, 0.1, 0.01 μM) (**Figure 5c**).

This yielded 21 rescuing molecules including 9/21 inhibitors whose assigned targets were JAK family kinases. Variability in rescue did not correlate with affinity for assigned JAK targets, which was generally in the nanomolar range (**Figure 5c**). The additional OKL hits did not detectably bind JAK family members (**Figure 5d**). We found that the rescuing agents, but not the non-rescuing agents, had micromolar ^{KS}Kds for multiple kinases other than JAK1-3/TYK2 including, ULK1-3, the numb associated kinases GAK, AAK1 and BIKE, and the entire DAPK family DAPK1-3 and DRAK1-2 that function in endocytosis, viral trafficking, and autophagy (**Figure 5e, Supplementary Figure 4c**)[43,44]. This is consistent with recent data showing that numb associated kinases contribute to the activity of baricitinib (Olumiant®), whose assigned targets are JAK1/2, against SARS-COV-2 infectivity, an indication for which baricitinib was recently approved[45].

The remaining OKL hits fell into three other groups: bromodomain inhibitors (these were in OKL since bromodomains are considered atypical kinase domains) that do not bind any kinases in our analysis; selective AKT/mTOR inhibitors; and promiscuous inhibitors that share affinity for MAP4 kinases (**Figure 5d-e, Supplementary Figure 4a-b**). Autophagy, the tightly controlled process by which cells selectively degrade and recycle proteins and organelles, is often dysregulated in AD[46]. The finding that combinations of ULK, DAPK, mTOR, and bromodomain inhibition reduces cdsRNA-mediated neuronal death suggests a role for autophagy: autophagy is downregulated by mTOR via ULK1, a key regulator of autophagy initiation[47] and BRD4 via transcriptional control of autophagy and

lysosome related genes[48]. Inhibition of MAP4 kinases, and not JAK inhibition, has recently been shown to promote neuroprotection against paclitaxel-induced peripheral neuropathy[49]. MAP4 kinases are also the assigned targets of prosetin[50], a drug currently in clinical trials for Amyotrophic Lateral Sclerosis (ALS). Together, these results suggest that MAP4 kinases are a node of convergence for multiple neurodegenerative conditions. This use case also illustrates the value of extending the OKL dataset in a context specific manner.

Other applications of OKL-affinity data

The second use case is an example of chemical genetics in which small molecules were used to dissect a cellular phenotype, in this case platinum-resistant high grade serous ovarian cancer (HGSOC). Platinum-based therapies are standard of care for HGSOC and commonly elicit tumor regression that is followed by resistance and recurrence[51]. We established a cell culture model of acquired cisplatin resistance by growing SNU8 cells in the presence of increasing concentrations of cisplatin until significant (but partial) resistance was achieved (**Figure 5f**). Screening parental and resistant SNU8 cells with the OKL at four concentrations (10 μM, 1 μM, 100 nM, and 10 nM) yielded 22 hit compounds (**Figure 5g**); rescreening was performed by collecting nine-point dose response curves in the absence of cisplatin. Thirteen hits were inhibitors of EGFR-family members (including 11 assigned EGFR inhibitors), four were MEK inhibitors and two were PI3K inhibitors (**Figure 5h-i, Supplementary Figure 5a**). These data demonstrate a requirement for EGFR signal transduction in cisplatin resistance, fulfilling our “chemical genetics” goal. They are also consistent with previous reports in cells and animal models [52,53]. However, EGFR inhibition has not proven to be clinically effective in the treatment of platinum-refractory HGSOC[54], but inhibition of kinases downstream of EGFR is another possibility as is inhibition of kinases not in the EGFR pathway but inhibited by hits in our screen such as GNE-3511 (a DLK inhibitor), CHIR-98014 (a GSK3 inhibitor), and UCN-01 (a broadly active compound).

In the third use case we looked for inhibitors of non-mammalian (pathogen) kinases present in the KINOMEscan panel. We identified nine inhibitors with ^{KS}Kd ≤ 100 nM for PKNB (**Figure 5j**), a serine threonine kinase essential for growth in *M. tuberculosis* (Mtb)[55–57]. We confirmed the potency of the top hits with 11-point Kd assays and found all had Kd < 15 nM (**Figure 5k**). When tested in Mtb growth-inhibition assays, pacritinib achieved half-maximal growth inhibition at 22.4 μM (95% confidence interval 19.9 μM – 25.3 μM) when butyrate was the carbon source (**Figure 5l**) but it was not effective under dormancy conditions[58] (**Supplementary Figure 5c**) consistent with the role of PKNB in Mtb growth. Since Mtb is treated with multiple drugs, we tested pacritinib in combination with eight antibiotics that are core components in standard of care treatment cocktails; we observed substantial synergy with isoniazid, pyrazinamide, and rifampicin (**Figure 5m**). Pacritinib is indicated for treatment of

myelofibrosis and thrombocytopenia[59] and its Cmax value is well below the effective concentration for inhibition of Mtb growth in vitro, but development of a pacritinib-like molecule based on existing medicinal chemistry series may be possible. We also identified 14 potent inhibitors (^{KS}Kd ≤ 100 nM) for the *P. falciparum* kinase PFCDPK1 and one for PFPK5 (**Supplementary Figure 5b**). PFPK5 is structurally similar to mammalian CDKs[60] and is most potently bound by PHA703887 whose assigned target is CDK2. This suggests that molecules intended to target human CDKs could be repurposed to develop anti-malaria drugs.

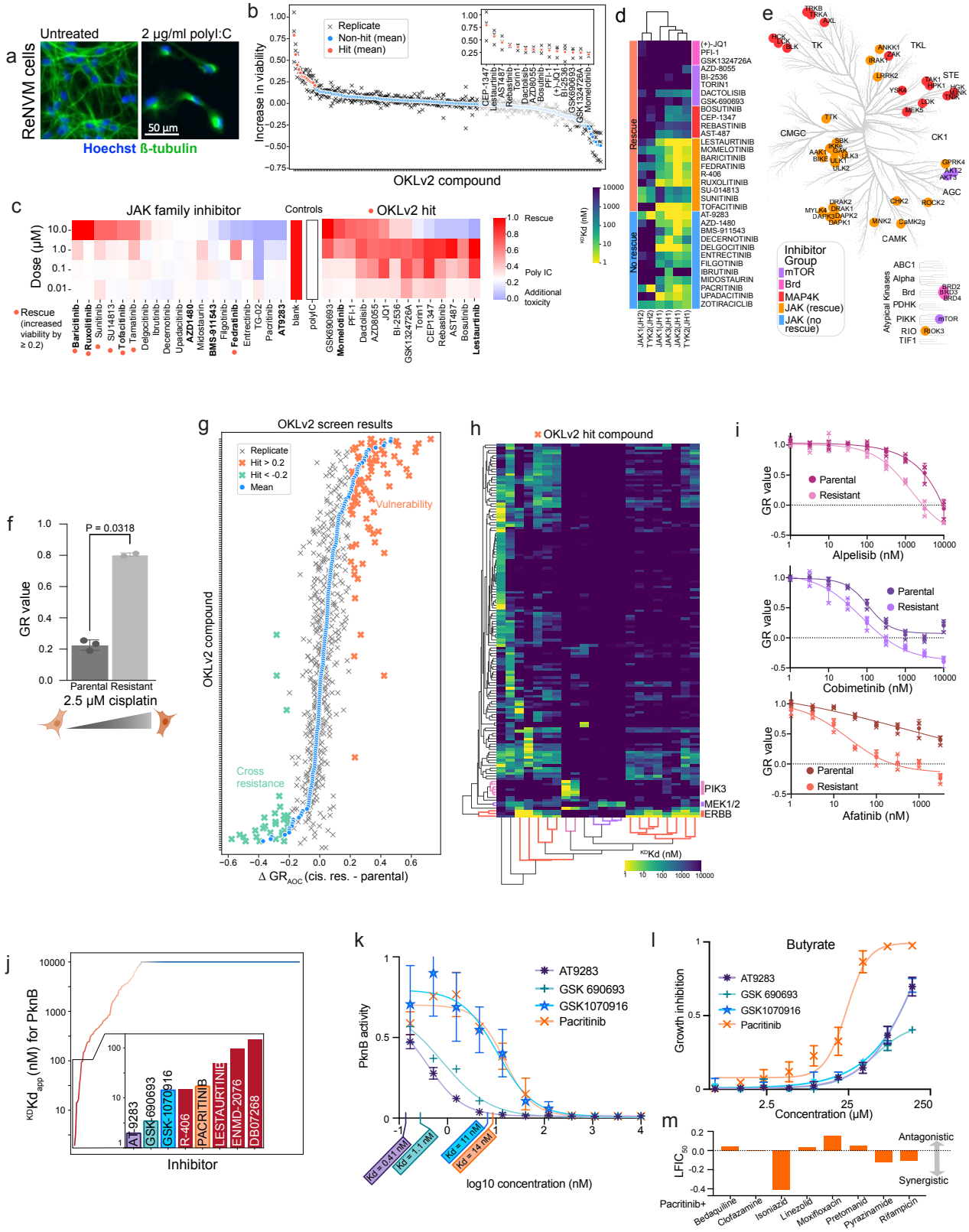

Figure 5: OKLv2 use cases. (a) Images of ReNcell® VM cells under control conditions (left) and treated with 2 µg/ml polyI:C (right) for seven days. Nuclei are shown in blue and ß-tubulin in green. The scale bar is 50 µm. **(b)** The change in percent viability conferred by the addition of each OKLv2 compound at 1 µM to treatment with 2 µg/ml polyI:C relative to polyI:C alone. The means of biological triplicates (denoted with x's) are shown as solid o's in red for hits, and blue for all others. **(c)** Heatmap

showing percent viability of ReNcell® VM cells treated with polyI:C and increasing concentrations of JAK inhibitors, and the OKL hits identified in **(b)**. **(d)** ^{KS}Kd values for the JAK family kinases for all inhibitors shown in **(c)** arranged by phenotype and common targets. **(e)** Common targets of rescuing agents shown on the kinome tree colored by the groups shown in **(d)**. **(f)** Bar graph showing GR values for parental and cisplatin resistant SNU8 cells treated with 2.5 μM cisplatin for 72 h. **(g)** Difference in GR_{AOC} between cisplatin resistant and parental SNU8 cells for each OKL inhibitor (n=3 biological replicates). Higher GR_{AOC} indicates sensitivity, while lower GR_{AOC} indicates resistance. Individual replicates are shown with x's, and the means with o's. Hits are marked in bold orange if more effective and in bold green if less effective in the resistant cells. **(h)** Clustermap of ^{KS}Kd values for hits that were more effective in resistant cells in at least two primary screens. Only kinases that were inhibited with ^{KS}Kd ≤ 100 nM by at least one hit are shown. **(i)** Dose response curves for inhibitors of targets identified in **(h)** for parental and cisplatin-resistant SNU8 cells. **(j)** ^{KS}Kd values for OKL compounds against PknB, the strongest inhibitors are shown in the inset bar graph. **(k)** 11-point Kd curves and Kd values for four of the top inhibitors from **(l)** for PknB. **(m)** Dose-dependent growth inhibition of Mtb treated with the same drugs in the butyrate growth condition. **(n)** Effect of pacritinib in combination with the drugs indicated on Mtb growth.

Recommendations on future KINOMEscans and interpreting existing data

A review of the literature suggests that it is rare to perform KINOMEscan assays at more than one dose, presumably due to cost. Eurofins suggests that hits be identified as having <35% of binding relative to a negative control regardless of the kinase or screening concentration. When we compared percent control values at each of our screening concentrations to Kds from ChEMBL (**Supplementary Figure 6a**) and evaluated the likelihood of correctly classifying a compound–target interaction across a range of percent control thresholds (*see Methods*, **Supplementary Figure 6b-c**). We found that the optimal screening concentration and threshold differed based on the objective of the screen and tolerance for false positive as opposed to false negative data (Type I and II errors; **Figure 6a**). For example, were one to screen ruxolitinib at 10 μM with the goal of identifying targets having Kd < 1000 nM, Eurofins standard threshold of 35% would return 94 false positives and two false negatives whereas our recommended cutoff 22% for this screening scenario returns 64 false positives and two false negatives (**Figure 6b-c**). This reduces false positives (by one-third) but given the amount of effort required to investigate off-targets, we also studied the value of performing KINOMEscans at two concentrations. To do this, we used Bayesian inference to estimate ^{KS}Kd values when two doses were screened (see **Supplementary Note, Supplementary Figure 6d, Figure 6d**) and found that 10 μM and 100 nM datapoints were optimal and were well correlated with four-point data (R^2 = 0.97, mean squared error = 0.094 for 2 dose vs. 4 dose ^{KS}Kd values, **Figure 6d-e**). We conclude that it is likely to be more efficient to screen compounds at two doses rather than one as a means of reducing type 1 error (**Figure 6e**).

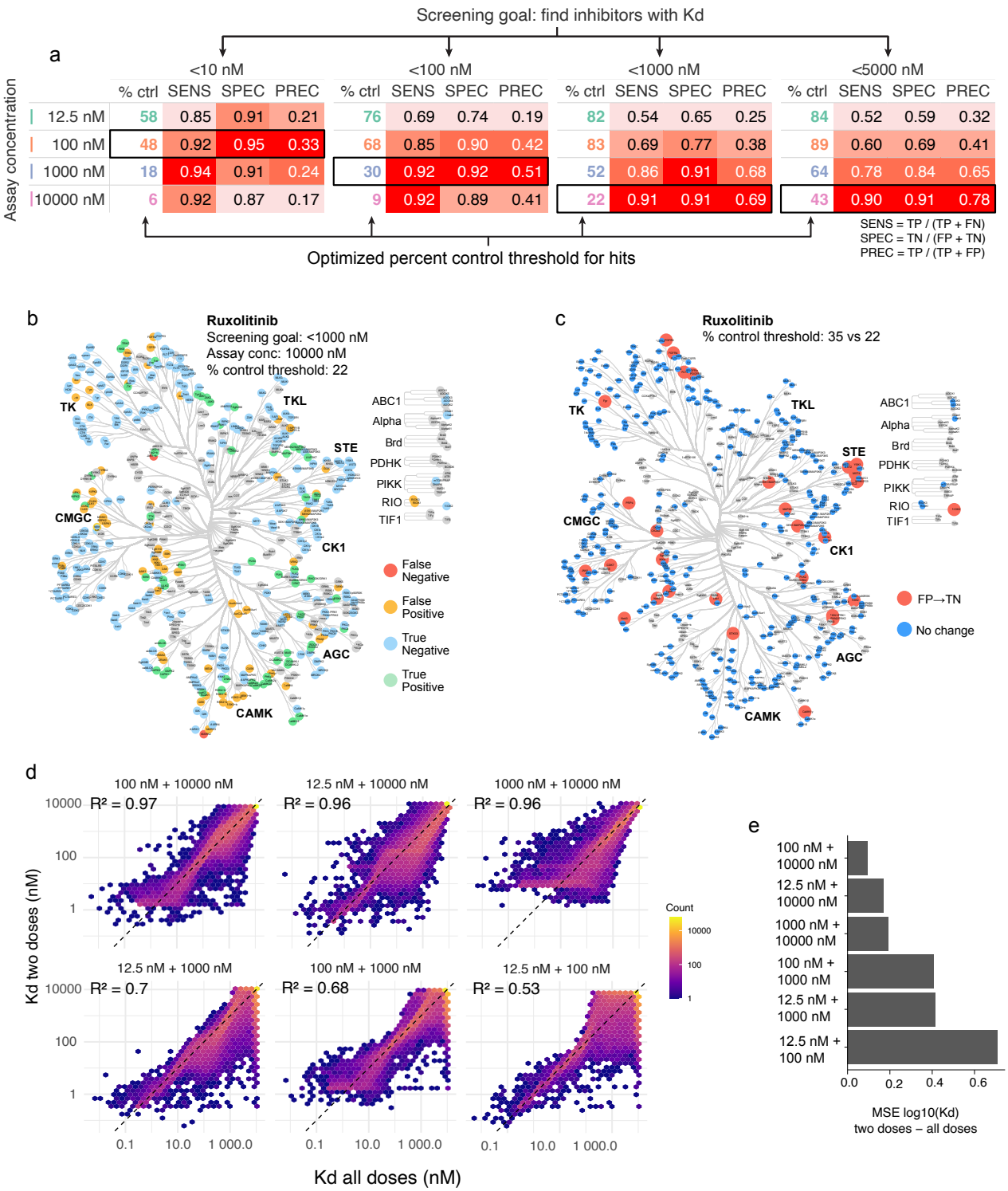

Figure 6: Recommendations for KINOMEscan analysis and interpretation. **(a)** Look-up table based on screening goal and assay concentration showing the sensitivity (SENS), specificity (SPEC) and precision (PREC) for the optimal cutoff values. **(b)** Kinome tree showing the classification of each kinase in a KINOMEscan of 10 μM ruxolitinib using a percent control threshold of 22. **(c)** Kinome tree showing the kinases that are misclassified using a 35% threshold and correctly classified using a 22% threshold. **(d)** Hexagonally binned scatter plots showing the ^{KS}Kd values estimated from all two dose pairs with respect to those estimated from all four doses. **(e)** Summary barplot of the mean squared error (MSE) of $\log_{10}(K_d)$ for all compound–kinase pairs for ^{KS}Kd values estimated from all two dose pairs.

DISCUSSION

The biological and clinical activities of molecules used as human therapeutics and tool compounds are commonly described in terms of a limited set of assigned targets, although it is generally understood that a substantial number of additional proteins are also bound. In some cases this can lead to striking changes in therapeutic focus and mechanism of action. Crizotinib, for example, was developed by Pfizer as an inhibitor of the cMET RTK but became a first in class inhibitor of ALK when its additional activities were discovered in cell line studies[61] and confirmed in clinical trials[62]. It is now possible to profile kinase inhibitors against the great majority of the human kinome using assays such as KINOMEscan, but such data has only sporadically become publicly available, particularly for therapeutics. In this paper we assemble a kinase inhibitor library (OKL) that balanced competing demands of compactness, chemical diversity, target coverage, and degree of clinical development. Performing KINOMEscan assays at four doses followed by Bayesian inference of binding constants (^{KS}Kd) yielded data that was well correlated with existing information in ChEMBL while filling in unknown quantities necessary for systematic analysis.

These data show that many kinase inhibitors, even those used as human therapeutics are potent but not particularly selective with a $PI_{max} < 0.2$, meaning that they bind multiple targets with similar affinities. Strikingly, for kinase inhibitors used as therapeutics, an assigned target is the *highest* affinity binder in only 23% of cases examined. We find no evidence that drugs that have succeeded in clinical development as opposed to those that were abandoned after Phase 1 are more selective. Moreover, the average selectivity of therapeutics has not appreciably increased over time, although the last few years have witnessed the development of some highly selective compounds. It does not follow that kinases inhibited by a particular compound are part of the biological or therapeutic mechanism of action, but it is noteworthy that these off targets include many understudied kinases whose functions are poorly understood. Thus, it is tempting to speculate that it is kinase inhibitor polypharmacology rather than selectivity that explains why this class of drugs has been so successful[63].

The availability of systematic kinase inhibitor activity data has multiple potential uses (thus, the data in this paper are freely available in raw and processed forms and have been incorporated in smallmoleculesuite.org). One striking finding is that there exists a subset of kinases that are substantially more promiscuous than the kinome as whole. In some cases, it is possible to rationalize this in terms of known structural properties (e.g. the DFG in and out conformations) but in many others we cannot, suggesting that additional structural studies are necessary. Unrecognized patterns of selective binding are also revealing. For example, potent binding of alectinib (assigned target ALK) to the liver-specific phosphorylase kinase isoform PHKG2 may explain the observed hepatoxicity of this compound. Not all potent ALK binders also bind PHKG2, however, suggesting that it might be possible to increase therapeutic index by considering PHKG2 as an anti-target during compound development[64].

Systematic affinity data also reveal multiple cases in which closely related kinases can be differentially targeted with existing chemical backbones, as well as cases in which this is not possible; such information can guide screening and medicinal chemistry efforts. The spectrum of small molecule binding data for each kinase also represents a different way to construct a kinome tree. Currently this is based on sequence alignment and presumed phylogeny, but a tree constructed by clustering small molecule data would be substantially more useful for drug discovery and mechanism of action studies. We estimate that a roughly two-fold expansion of the OKL library to include the latest clinical and pre-clinical traditional kinase inhibitors, PROTACs and molecular glues[65] would make this possible and is well within the capacity of an academic lab with dedicated funding. The current paper includes computational tools and practical guidelines to guide such an effort, or any other use of KINOMEscan screening, that go beyond what the vendor (Eurofins) recommends.

The possibility of instantiating the OKL in this paper using commercial resources makes it feasible to use it for screening. Moreover, in cases in which an inhibitor with multiple targets induces a desirable phenotype, an OKL screen can help to narrow down the list of functional targets even in settings in which RNAi and similar genetic approaches are challenging. For example, in the work of Petrova et al[49]. a multi-targeting kinase inhibitor, KW-2449, was found to be neuroprotective against paclitaxel-induced peripheral neuropathy and an OKL screen suggested that STE20 kinases play a critical role.[49] In this paper we use OKL to screen for potential neuroprotective agents in a model of Alzheimer's disease and platinum-resistant ovarian cancer. In each case, the availability of systematic binding data made the screens much easier to interpret because they revealed common and, in some cases, unrecognized off-target activities. These studies also demonstrated that it is possible to selectively expand the OKL and associated data to include new molecules focused on specific kinase subsets (in our case JAK family inhibitors).

Drugs targeting kinases are indicated for many conditions, and kinase inhibition remains an area of intense focus in academia and pharma. Despite decades of effort, moving new molecules through development and predicting which are most likely to make good therapeutics remains challenging. The current work challenges some common assumptions about what makes a good human therapeutic, while providing an approach to maximizing the information that can be obtained from phenotypic screens.

Acknowledgements

We thank ICCB-L for compound management, and J. Tefft and C. Dessauges for helpful discussions, and manuscript editing, N. Moret for OKL compound selection, H. D'Erasmo for testing in Mtb through the DiaMOND platform at Tufts University. This work was primarily funded by the DARPA PANACEA program, award HR0011-19-2-0022, the NIH Illuminating the Druggable Genome Grant U24-DK116204, and the Ludwig Center at Harvard. It was also supported by NSF 22-599, EPSCoR RII Track-1, Award Number DQDBM7FGJPC5 (RC).

Author Contributions

Conceptualization: CEM, CH and PKS; Methodology: CEM, CH, KAS, NC, CV, MC, SR, RC and BMG; Investigation: CEM, CH, CV and MC; Formal analysis: CEM, CH and BMG; Resource: CEM, CH and PKS; Visualization: CEM, CH and RC; Funding acquisition: RC and PKS; Supervision: CEM, BA, MWA, RC, BMG and PKS; Writing – original draft: CEM, CH and PKS; Writing – review & editing: CEM, CH, BMG and PKS.

Conflicts of Interest

The authors declare the following competing financial interest(s): PKS is a co-founder and member of the BOD of Glencoe Software, a member of the BOD for Applied Biomath, and a member of the SAB for RareCyte, NanoString, and Montai Health; he holds equity in Glencoe, Applied Biomath, and RareCyte. PKS is a consultant for Merck, and the Sorger lab has received research funding from Novartis and Merck in the past five years.

METHODS

KINOMEscan assays

Small molecule inhibitors were purchased from commercial vendors. Stock solutions were prepared in dDMSO at 10 mM for all compounds with the following exceptions due to limitations in solubility: CAY10561 5 mM, CHIR-98104 2 mM, gedatolisib 4 mM, and indirubin 3 mM. Inhibitors were arrayed in 96 well plates, 100 µl per inhibitor, and sent to Eurofins for scanMAX profiling. scanMAX profiling was performed in two batches: in the first batch, scans were performed at 10 µM and 100 nM; scans in the second batch were performed at 1 µM and 12.5 nM concentrations. Due to space constraints on assay plates, a subset of inhibitors was only screened in the first batch and therefore only have data points at 10 µM and 100 nM. For each concentration of each inhibitor, a percent of control value was returned for 406 WT kinases and 59 mutant kinases and three non-mammalian kinases for analysis.

Inhibitors were sent to Reaction Biology for follow-up IC50 assays, performed in duplicate at 10-dose points (HotSpot™ radiometric assays, with 10 µM ATP), or to Eurofins for follow-up Kd assays performed in duplicate at 11-dose points (KdELECT®) depending on assay availability.

Quality control of KINOMEscan data

To assess the quality of the dataset, we first examined its internal consistency by plotting the percent control values in four-point dose response curves for every inhibitor-kinase pair and classifying their shapes. Eurofins recommends using a cutoff of 35% control for hits. We defined five classes: *non-binding*, no measurements below 35% control; *binding*, two or more measurements below 35% control,

all measurements concordant; *weakly binding (high confidence)*, one measurement below 35%, p<0.1 for a linear model fit to the dose response curve; *weakly binding (low confidence)*, none of the above apply (these are usually curves where the 10 μM data point is the only data point below 35%); and *discordant*, one measurement below 35% control, one measurement, at a higher concentration, above 35% and at least two-fold higher than a previous value (**Supplementary Figure 1a**). We found that 73% of the dose responses measured were classified as non-binding in line with the library consisting primarily of inhibitors that were designed to be selective. However, 2% of the ~90k dose response relationships were classified as discordant, accounting for 6% of the data points when non-binding curves are excluded (**Supplementary Figure 1b**). When we took a closer look at the discordant class, particular inhibitors and kinases accounted for a disproportionate number of these aberrant curves suggesting that there were systematic errors in the dataset (**Supplementary Figure 1c, d**). The dose response relationships for these kinases and inhibitors showed clear batch effects (the percent control values for the 1 μM and 12.5 nM data points were often lower than the 10 μM and 100 nM data points) (**Supplementary Figure 1e-g**, left panels). Kinases are pooled in KINOMEscan assays so the worst performing kinases were likely multiplexed during data collection. Therefore, we repeated the assays for all inhibitors for the seven worst performing kinases (**Supplementary Figure 1d**, bold font), and for the 12.5 nM and 1000 nM concentrations of erlotinib (the worst performing inhibitor). This markedly improved the concordance of the dose responses for those conditions (**Supplementary Figure 1e-g**, right panels) and reduced the overall fraction of discordant dose responses to 1% of the total dataset (4% if non-binding curves are excluded) (**Supplementary Figure 1h**). The remaining discordant dose responses are broadly distributed across kinases and inhibitors suggesting that any remaining errors were random (**Figure 2g**). Discordant dose responses have been removed from all analyses. There were an additional 300 data points that were initially reported as 100% control (no binding) that were qPCR dropouts (Eurofins provided this list, but it is not routinely shared). These data points have also been excluded.

Inhibitor type assignments were sourced from the literature as much as possible. The relative affinity of kinase inhibitors for WT or mutant ABL1 in its nonphosphorylated vs. phosphorylated states has been previously shown to distinguish type I (no preference for activation state) from type II inhibitors (preference for the nonphosphorylated state)[7,66]. We used this approach for inhibitors with Kd < 3 μM for any ABL1 target.

KINOMEscan-derived Kd values (^{KD}Kd), target affinity spectra, and partition index calculations

To estimate dissociation constants (Kd) and Hill slopes from KINOMEscan dose-response data, we implemented a Bayesian hierarchical model using PyMC (version 5.25.1) with the nutpie sampler (version 0.15.2). The model relates compound concentration to the observed percent control values through a standard dose-response relationship. The mean response at a given dose was modeled using a variation of the four-parameter Hill equation:

$$\mu(c) = 100 - \frac{100}{1 + \left(\frac{K_d}{c}\right)^h}$$

where c is the compound concentration, K_d is the dissociation constant, and h is the Hill slope coefficient. This formulation represents the percent of kinase activity remaining (percent control) as a function of inhibitor concentration.

The measurement error was modeled as heteroscedastic, with variance proportional to the predicted response. We used an empirically derived error model:

$$\sigma(\mu) = max(0.15\mu - 0.043,1)$$

where σ is the standard deviation of the measurement error at predicted response μ. This error model was derived from technical reports provided by the vendor and accounts for the observation that measurement variability increases with higher percent control values, while maintaining a minimum error floor of 1% control.

We employed weakly informative priors to constrain parameters to biologically plausible ranges while allowing the data to dominate inference. $\log(K_d) \sim \mathcal{N}(\log(10^{-6}), 3))$, corresponding to a log-normal prior on K_d centered at 1 μM with wide variance spanning nanomolar to millimolar affinities; and $\log(h) \sim \mathcal{N}(0,0.5)$ corresponding to a log-normal prior on the Hill slope centered at 1

The observed percent control values were modeled as:

$$y_i \sim \mathcal{N}(\mu(d_i), \sigma(\mu(d_i)))$$

where y_i is the observed percent control at dose d_i

For each compound-kinase pair, we sampled from the posterior distribution using the No-U-Turn Sampler (NUTS) as implemented in the nutpie package. We ran 4 independent Markov chains, each with 1,000 tuning iterations and 2,000 sampling iterations, for a total of 8,000 posterior samples per compound-kinase pair. Convergence was assessed using the Gelman-Rubin statistic ($\hat{R}$), with $\hat{R} < 1.01$, considered indicative of convergence. Point estimates for K_d and Hill slope were obtained as posterior means, with uncertainty quantified using posterior standard deviation and 95% highest density intervals.

To facilitate comparisons with previous analyses, we converted the $^{KD}Kd_{app}$ values to target affinity spectra (TAS): $^{KD}Kd_{app}$ > 10 μM corresponds to a TAS value of 10; $^{KD}Kd_{app}$ between 1 μM and 10 μM to TAS 3; $^{KD}Kd_{app}$ between 100 nM and 1 μM to TAS 2; and $^{KD}Kd_{app}$ < 12.5 corresponds to TAS 1.

We calculated the partition index[21,67] (PI) for each kinase and inhibitor pair using our $^{KD}Kd_{app}$ values (equation 3).

Equation 1: PI = 1/Kd(target of interest) / sum (1/Kd1…1/Kdn)(all targets).

OKLv2 screening in ReNcell® VM cells

ReN VM cells were maintained in their recommended growth conditions in ReNcell® NSC maintenance media (EMD Millipore, Danvers MA), supplemented with 20 ng/ml rhEGF (Millipore Sigma, Burlington, MA), 20 ng/ml FGF (Millipore Sigma, Burlington, MA); 5% CO_2, 37˚C, on growth factor reduced Matrigel (Corning, Corning, NY). Prior to drug treatments, cells were differentiated on 10 cm plates by removing growth factors from the media for seven days. Cells were then removed from the plates using accutase (EMD Millipore, Danvers, MA) and plated in 96 well plates and allowed to differentiate for another seven days. Media was changed twice per week during differentiation. For OKLv2 screening (final concentration 1 μM), drug treatments were added by acoustic transfer using an

ECHO 655 (Beckman Coulter, Brea, CA) at the ICCB-L screening facility one hour prior to the addition of 2 µg/ml (final concentration) of poly(I:C) HMW (Invivogen, San Diego, CA). After four (replicate 1) or six (replicates 2 and 3) days, an equal volume of Cell Titer Glo 2.0 (Promega, Madison, WI) was added to each well, incubated at room temperature with rocking for 10 min. and luminescence was measured with a Synergy H1 (BioTek, Winooski, VT) plate reader. Validation experiments were performed in the same way except drug treatments were delivered with a D300 digital drug dispenser, and data were collected after seven days.

Dose response measurements in ovarian cancer cells

SNU8 ovarian cancer cells were maintained in RPMI-1640 supplemented with 2 mM L-glutamine, 25 mM HEPES, 10% fetal bovine serum and 1% penicillin/streptomycin at 37˚C and 5% CO2. Cells were identity validated by short tandem repeat profiling[68] and verified to be free from mycoplasma. Cisplatin-resistant cells were generated by adding cisplatin to the growth media starting at 0.5 µM. The dose was escalated incrementally, as the cells allowed, until they were stable in the presence of 3 µM cisplatin (approximately six months). For all dose response measurements, the parental and resistant cells were plated in 384 well CellCarrier ULTRA plates (Perkin Elmer, Waltham, MA) at 750 cells per well in 60 µl media, in the absence of cisplatin. Cells were allowed to adhere for 24 h prior to drug treatment. Drug treatments (final concentrations of 10, 1, 0.1, and 0.01 µM) were delivered via pin transfer with a custom E2C2515-UL Scara robot (Epson, Long Beach, CA) coupled to stainless steel pins (V&P Scientific, San Diego, CA) from 1000x library plates at the ICCB-L screening facility at Harvard Medical School for the screens, and using a D300 digital drug dispenser in nine-point half-log dilution series for validation experiments (Hewlett-Packard, Palo Alto, CA). At the same time that drugs were added, a time = 0 plate was stained and fixed using the Deep Dye Drop protocol[69]. Following six days in drug, all remaining assay plates were stained and fixed using the Deep Dye Drop protocol. In brief, live cells were stained with LIVE/DEAD Red (LDR) (Thermo Fisher, Waltham, MA), and pulsed with EdU (Lumiprobe, Waltham, MA) for one hour in a solution of 10% Optiprep™ (a density gradient medium) (Sigma, St. Louis, MO) in phosphate buffered saline (PBS). Cells were then fixed with 4% formaldehyde prepared in 20% Optiprep™ for 30 min. The addition of sequentially denser solutions enables staining and fixation without the need for any aspirate or wash steps thus preserving cells susceptible to loss, reducing the number of protocol steps, and sparing reagents and costs[69]. Following fixation, cells were permeabilized with 0.5% Triton X-100 for 15 min., the EdU was labeled with cy3-azide (Lumiprobe, Waltham, MA) using Click chemistry for 30 min., cells blocked in Odyssey buffer (Li-COR Biosciences, Lincoln, NE) for one hour at room temperature, and finally stained overnight with Hoechst (1:5000, Thermo Fisher, Waltham, MA) and an alexa 488 conjugated anti-phospho histone H3 antibody prepared in Odyssey (1:2000, Cell Signaling Technologies, Danvers, MA).

Stained and fixed cells were imaged with an ImageXpress Micro-Confocal (IXM-C) high throughput microscope equipped with a plate hotel and robotic arm (Molecular Devices, San Jose, CA). Four fields of view were imaged per well with a 10x objective for full well coverage. Image analysis was performed with MetaXpress software (version 6.5.3.427, Molecular Devices, San Jose, CA): nuclei were segmented, and nuclear masks were defined based on the Hoechst signal. The nuclear mask was dilated to create a ring mask, and the intensity of each signal in each mask was measured. Local background was accounted-for by subtracting the intensity of each marker in the ring mask from the nuclear mask. Objects touching the edge of the images were excluded from analysis. Analysis of the raw feature data was performed using custom scripts (https://github.com/datarail/DrugResponse/wiki)[69]. The integrated Hoechst intensity was used for DNA content quantification, EdU intensity for S-phase

cells, and phospho-histone H3 intensity for M-phase cells. LDR signal was used to identify dead cells. Growth rate inhibition (GR) values and metrics were calculated as defined by the number of viable cells at the time of drug treatment (t=0), and at endpoint under untreated and treated conditions[70]. A compound was considered to induce a stronger effect in the cisplatin resistant cells if the difference between the area over the GR curve (GR_{AOC}) was at least 0.2 lower than for the same treatment in the parental controls. Compounds that met this condition in at least two biological replicates of the screen were considered hits.

Molecular Dynamics Simulations

We performed molecular dynamics (MD) simulations to investigate the structural and energetic basis of CLK-inhibitor interactions for both apo and holo conformations of CLK1 (PDB 6Q8K), CLK2 (PDB 6FYI), CLK3 (PDB 6RCT), and CLK4 (PDB 6FYV) with eight inhibitors (64 simulations in total) using the GROMACS[71,72] molecular simulation platform. We constructed two system configurations: (1) *apo-CLK systems*, where the inhibitor was positioned near CLK but outside the binding pocket, and (2) *holo-CLK systems*, where the inhibitor was positioned within the CLK binding pocket. We applied the charmm36 force field[73] to model the systems and parameterized the inhibitors using the Automated Topology Builder (ATB)[74]. To prepare the initial system configurations, we solvated CLK-inhibitor in a cubic simulation box with the TIP3P water model and added Na^+ or Cl^- ions to neutralize the charge and avoid artifacts in long-range electrostatics calculations. We carried out energy minimization using the steepest descent method[75], followed by a 100-ps equilibration phase under the canonical ensemble (NVT) at 300 K, where we restrained the protein's heavy atoms. We then carried out isothermal-isobaric equilibration (NPT) at 300 K and 1 bar using the Parrinello-Rahman barostat[76]. Finally, we conducted production MD simulations for 500 ns under the same thermodynamic conditions, using a time step of 2 fs. All equilibration and production runs used the leapfrog integrator[77]. We imposed periodic boundary conditions in all dimensions and calculated long-range electrostatics using the Particle Mesh Ewald (PME) method[78]. To ensure consistency, the same force field parameters and simulation protocols were applied across all systems. Predicted scores were normalized to the highest absolute value of all predictions.

Dose response measurements in *M. tuberculosis*

Aliquots of pacritinib, AT9283, GSK690693, and GSK1070916 (200 µl at 10 mM in DMSO) were sent to the Aldridge lab at Tufts University. Dose centering curves were performed for *M. tuberculosis* (Mtb) in standard, butyrate, high cholesterol, acidic, and dormancy growth conditions[58].

Supplementary Note

Bayesian Estimation of Dissociation Constants from four- and two-dose KINOMEscan Dose-Response Data

The Eurofins KINOMEscan platform provides a cost-effective competitive binding assay for profiling compound affinity across nearly the entire human kinome. In this study, we profiled each of the 192 OKL compounds at four concentrations (12.5, 100, 1000, and 10,000 nM), generating 89,856 four-point dose-response curves. Conventionally, KINOMEscan data are assessed at a single concentration using a threshold of <35% control remaining to classify a compound–kinase pair as a 'hit.' While straightforward, this binary classification discards quantitative information about binding affinity and provides no estimate of the dissociation constant (K_d). To extract more information from these dose-response data, we utilized a Bayesian inference framework that fits a sigmoidal dose-response model to the observed percent control values, yielding posterior distributions over K_d and Hill slope for each compound–kinase pair.

Model Specification

We model the relationship between inhibitor concentration and the observed percent of control remaining using a four-parameter Hill equation. Let c denote the compound concentration, K_d the dissociation constant, and h the Hill slope coefficient. The mean predicted response is:

$$\mu(c) = 100 - 100 / (1 + (K_d / c)^h)$$

This formulation represents the percent of kinase activity remaining as a function of inhibitor concentration: at low concentrations relative to K_d, the predicted response approaches 100% (no inhibition), and at high concentrations it approaches 0% (complete inhibition).

Measurement error was modeled as heteroscedastic, with the standard deviation proportional to the predicted response. We employed an empirically derived error model based on technical reports from Eurofins:

$$\sigma(\mu) = \max(0.15\mu - 0.043, 1)$$

This captures the observation that measurement variability increases with higher percent control values while maintaining a minimum error floor of 1% control. The observed percent control values y_i at each dose d_i were modeled as normally distributed around the predicted mean with standard deviation given by the error model.

Prior Distributions

We specified weakly informative priors to constrain parameters to biologically plausible ranges while allowing the data to dominate inference. For the dissociation constant, we placed a log-normal prior centered at 1 μM with wide variance:

$$\log(K_d) \sim N(\log(10^{-6}), 3)$$

This prior spans a broad range from sub-nanomolar to millimolar affinities, accommodating the full spectrum of biologically relevant dissociation constants. For the Hill slope, we used:

$$\log(h) \sim N(0, 0.5)$$

corresponding to a log-normal prior centered at a Hill slope of 1, consistent with standard single-site binding kinetics, while allowing moderate deviations.

Posterior Inference

For each compound–kinase pair, we sampled from the posterior distribution using the No-U-Turn Sampler (NUTS) as implemented in the nutpie package with PyMC (version 5.25.1). We ran four independent Markov chains, each with 1,000 tuning iterations and 2,000 sampling iterations, yielding 8,000 posterior samples per pair. Convergence was assessed using the Gelman–Rubin statistic ($\hat{R}$), with $\hat{R} < 1.01$ considered indicative of adequate convergence. Point estimates for K_d and Hill slope were obtained as posterior medians, and uncertainty was quantified using posterior standard deviations and 95% highest density intervals (HDIs). The full implementation is available as a Python command-line tool that supports parallel execution across compound–kinase pairs with results stored in a SQLite database for reproducibility and seamless continuation after interrupted runs.

Validation Against ChEMBL Reference Data

To assess the accuracy of our Bayesian K_d estimates (denoted ${}^{KS}K_d$), we compared them to K_d values deposited in ChEMBL for overlapping compound–kinase pairs where full dose-response curves had been collected using orthogonal assay platforms. We observed good agreement between the four-dose KINOMEscan-derived K_d values and the ChEMBL reference values ($R^2 = 0.91$; Figure 1f), demonstrating that four concentration points spanning four orders of magnitude are sufficient to estimate dissociation constants with high fidelity using the Bayesian framework.

Minimum Number of Doses Required for Reliable K_d Estimation

Given the cost of kinome-wide profiling, we investigated whether fewer than four concentration points could yield reliable K_d estimates. We systematically evaluated all six pairwise combinations of the four assay concentrations (12.5, 100, 1000, and 10,000 nM) by fitting the Bayesian model to each two-dose subset and comparing the resulting K_d estimates to those obtained from the full four-dose data (**Figure 6a**).

As an illustrative example, **Supplementary Figure 6a** shows dose-response fits for lenvatinib binding EPHB6 across all dose combinations. The four-dose fit (all doses) yields a K_d of 35 nM with a narrow 95% HDI. Two-dose subsets that include concentrations spanning the widest dynamic range—particularly 100 nM + 10,000 nM—produce K_d estimates (41 nM) and credible intervals closely matching the four-dose fit. In contrast, subsets comprising closely spaced concentrations (e.g., 12.5 nM + 100 nM) yield wider credible intervals and slightly different point estimates, reflecting the reduced information content of narrowly spaced doses.

To quantify performance across the entire dataset, we compared the two-dose and four-dose Kd estimates using hexagonally binned scatter plots and computed the R^2, showing that certain assay concentration combinations perform better for different ranges of Kd estimation (**Figure 6a**). To quantify the estimation error when going from four to two doses, we computed mean squared error (MSE) of $\log_{10}(K_d)$ for all compound–kinase pairs (**Figure 6b**). The combination of 100 nM + 10,000 nM achieved the best overall performance, with $R^2 = 0.97$ and MSE = 0.094. This was closely followed by 12.5 nM + 10,000 nM ($R^2 = 0.96$, MSE = 0.168) and 1000 nM + 10,000 nM ($R^2 = 0.96$, MSE = 0.193) (**Figure 6a-b**. Dose pairs that did not include the highest concentration (10,000 nM) performed substantially worse, with MSE values 2–7-fold higher.

The strong performance of the 100 nM + 10,000 nM combination can be understood intuitively: these two concentrations bracket the K_d values of most compound–kinase pairs in the dataset,

providing information about both the upper and lower plateaus of the dose-response curve. Concentrations that are both above or both below the K_d provide redundant information about one plateau, yielding poorly constrained estimates. Based on these results, we recommend that future KINOMEscan experiments adopt a minimum two-dose design at 100 nM and 10,000 nM when full four-dose profiling is not feasible due to cost constraints.

Advantages of the Bayesian Approach

For comparison to an alternative approach, we calculated Kd values for each concordant dose response that crossed 50% control by interpolating from a linear relationship between the data points on either side of the 50% mark. We assigned curves that never reached 50% control Kd > 10 μM (highest screening dose), and those that were below 50% control at all screening concentrations Kd < 100 nM or Kd < 12.5 nM depending on the lowest dose screened for each inhibitor. While the correlation between these Kd estimates and data in ChEMBL was good (R=0.88), we could not estimate relative affinities below our lowest screening concentration (**Supplementary Figure 1h**). Answers to the common questions of (i) what is the highest affinity target of an inhibitor? and (ii) what target is most selectively bound by an inhibitor? were difficult to answer since they were multi-way ties. For example, a potent multi-targeting inhibitor like dasatinib, inhibits 48 kinases with Kd < 12.5 nM, resulting in a 48-way tie for PI_{max}. With the Bayesian approach described here, we can see that dasatinib most selectively inhibits EPHA2 with PI_{max} = 0.32 and ^{KS}Kd = 0.035 nM.

The Bayesian framework described here offers several advantages over conventional threshold-based analysis of KINOMEscan data. Most fundamentally, each K_d estimate is accompanied by a full posterior distribution, from which 95% highest density credible intervals are derived. This enables downstream analyses to propagate uncertainty rather than relying on point estimates alone, providing a principled measure of confidence for each compound–kinase interaction. The weakly informative priors further serve as a form of regularization, shrinking K_d estimates derived from noisy or sparse data toward biologically plausible values. This is particularly important for compound–kinase pairs near the limit of detection, where conventional curve-fitting approaches may yield unstable or biologically implausible estimates.

Because the model encodes the expected shape of the dose-response relationship through the Hill equation and prior distributions, it can also estimate K_d values that fall outside the range of tested concentrations. Compounds with K_d < 12.5 nM (below the lowest tested concentration) or K_d > 10,000 nM (above the highest) can still be assigned meaningful, albeit less certain, affinity estimates, with broader credible intervals that appropriately reflect the increased uncertainty. This capacity for extrapolation has practical consequences for selectivity analysis: quantitative K_d estimates across the full affinity range enable the computation of continuous selectivity metrics such as the partition index (PI), which represents the fraction of compound bound to each kinase in a theoretical equimolar mixture. By leveraging the full range of estimated affinities, including sub-nanomolar K_d values extrapolated below the lowest assay concentration, the partition index substantially improves the resolution of selectivity profiles relative to threshold-based hit calling, which treats all sub-threshold interactions as equivalent.

Finally, as demonstrated above, the Bayesian framework yields reliable K_d estimates from as few as two concentration points, enabling significant cost reductions without substantially compromising data quality. This makes kinome-wide profiling more accessible and scalable for large compound collections. Notably, numerous past KINOMEscan experiments have already been performed at two doses; these existing datasets could benefit from reanalysis using the approach described here.

SUPPLEMENTARY FIGURES

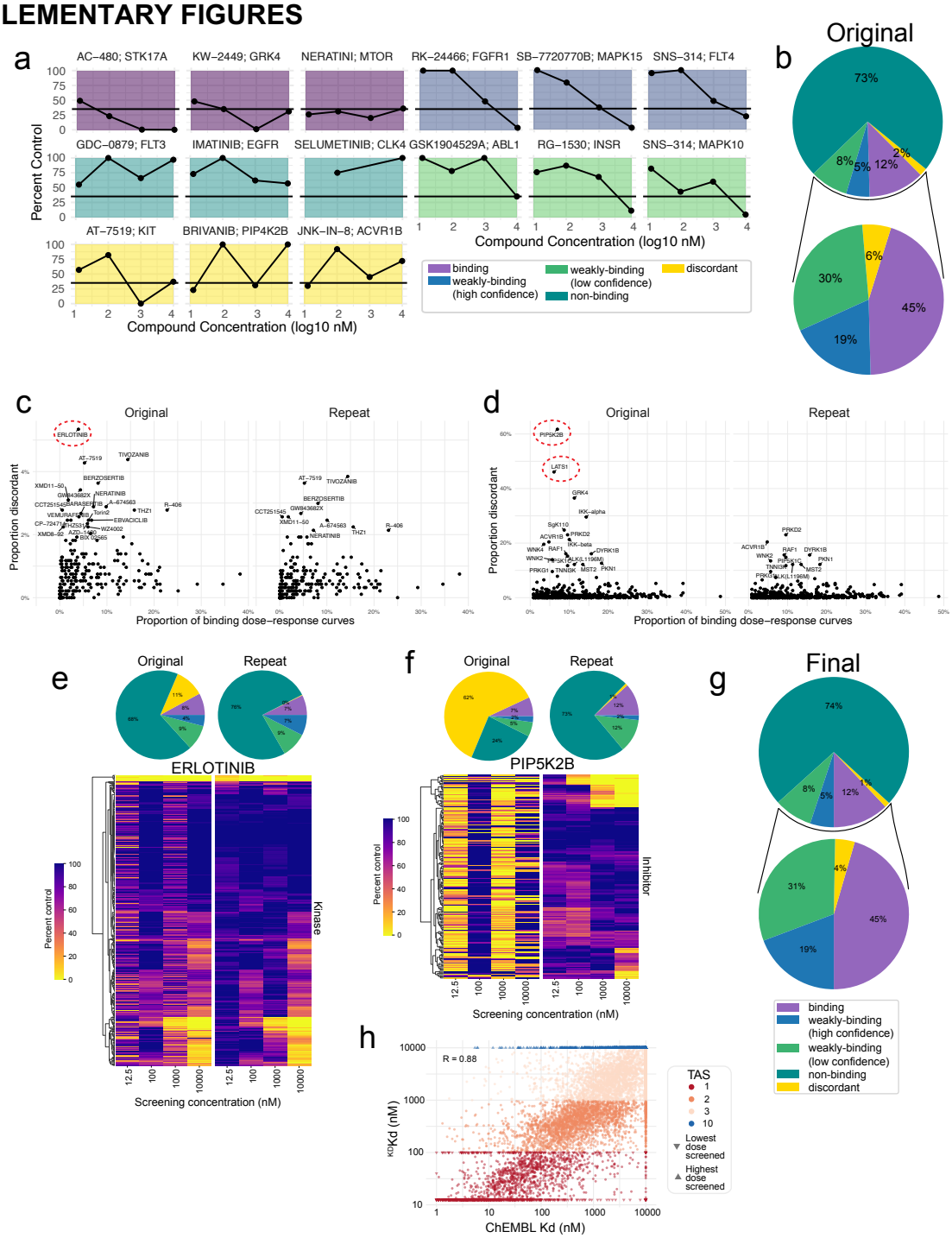

Supplementary Figure 1: **(a)** Examples of percent control dose response curves for each class as indicated. Discordant dose responses were excluded from the dataset. **(b)** Pie charts showing the fraction of dose responses that fall into each class, and the distribution of dose response classes when the confirmed non-binding class is excluded. **(c)** Scatter plots showing the fraction of discordant dose response curves with respect to the fraction of binding dose response curves for all inhibitors and **(d)** for all kinases in the original dataset (left plots) and in the final post-QC dataset (right plots). **(e)** Heatmaps showing % control values for erlotinib against all kinases at all concentrations tested, and pie charts summarizing the fraction of dose responses in each class pre- and post-QC. **(f)** Heatmaps showing % control values for PIP5K2B and **(g)** Pie charts showing the fraction of dose responses that fall into each class, and the distribution of dose response classes when the confirmed non-binding class is excluded. **(h)** Scatterplot comparing ^{KS}Kd values estimated by linear interpolation to those previously available in ChEMBL. Data points are colored by TAS value, and the values for each compound's assigned target(s) are outlined in black.

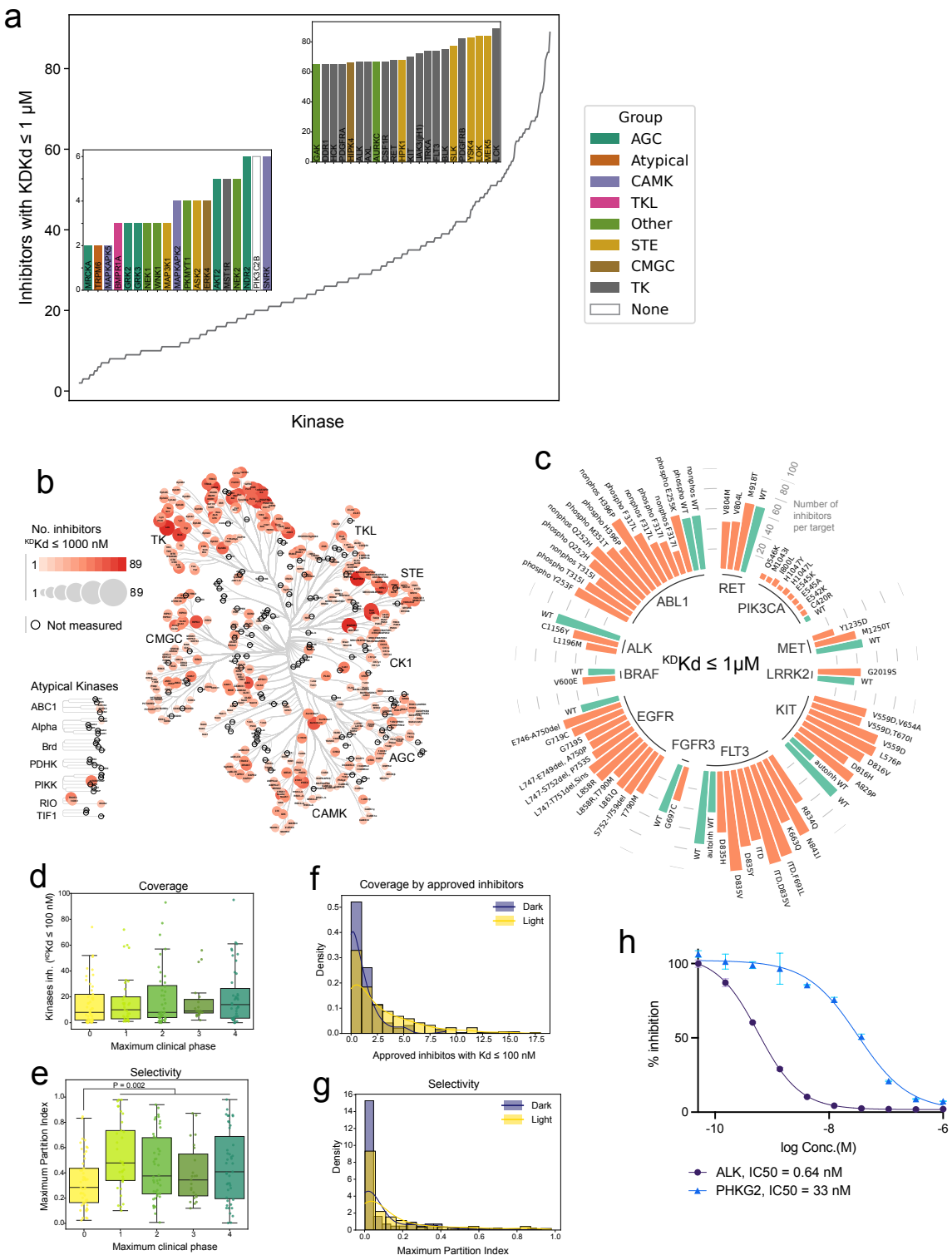

Supplementary Figure 2: **(a)** The number of inhibitors with ^{KS}Kd ≤ 1 μM per kinase. The inset plot shows the top 20 kinases most widely inhibited by OKL compounds colored by group. **(b)** The number of OKL inhibitors (^{KS}Kd < 1 μM) per kinase shown on the kinome tree by the size and intensity of the markers. **(c)** Radial bar plot showing the number of OKL inhibitors with ^{KS}Kd ≤ 1 μM for all mutant kinases (red bars) assayed in the KINOMEscan panel. WT kinases are indicated with blue bars. **(d)** Boxplot showing the number of kinases per inhibitor with ^{KS}Kd ≤ 100 nM by maximum stage of clinical development reached. **(e)** Boxplot showing the maximum partition index for each OKL inhibitor by maximum stage of clinical development reached. P-value is from a one-way ANOVA with Tukey's correction for multiple comparisons. **(f)** Histogram of the maximum partition indices for all dark and light kinases. KDE lines are overlaid for visualization only.

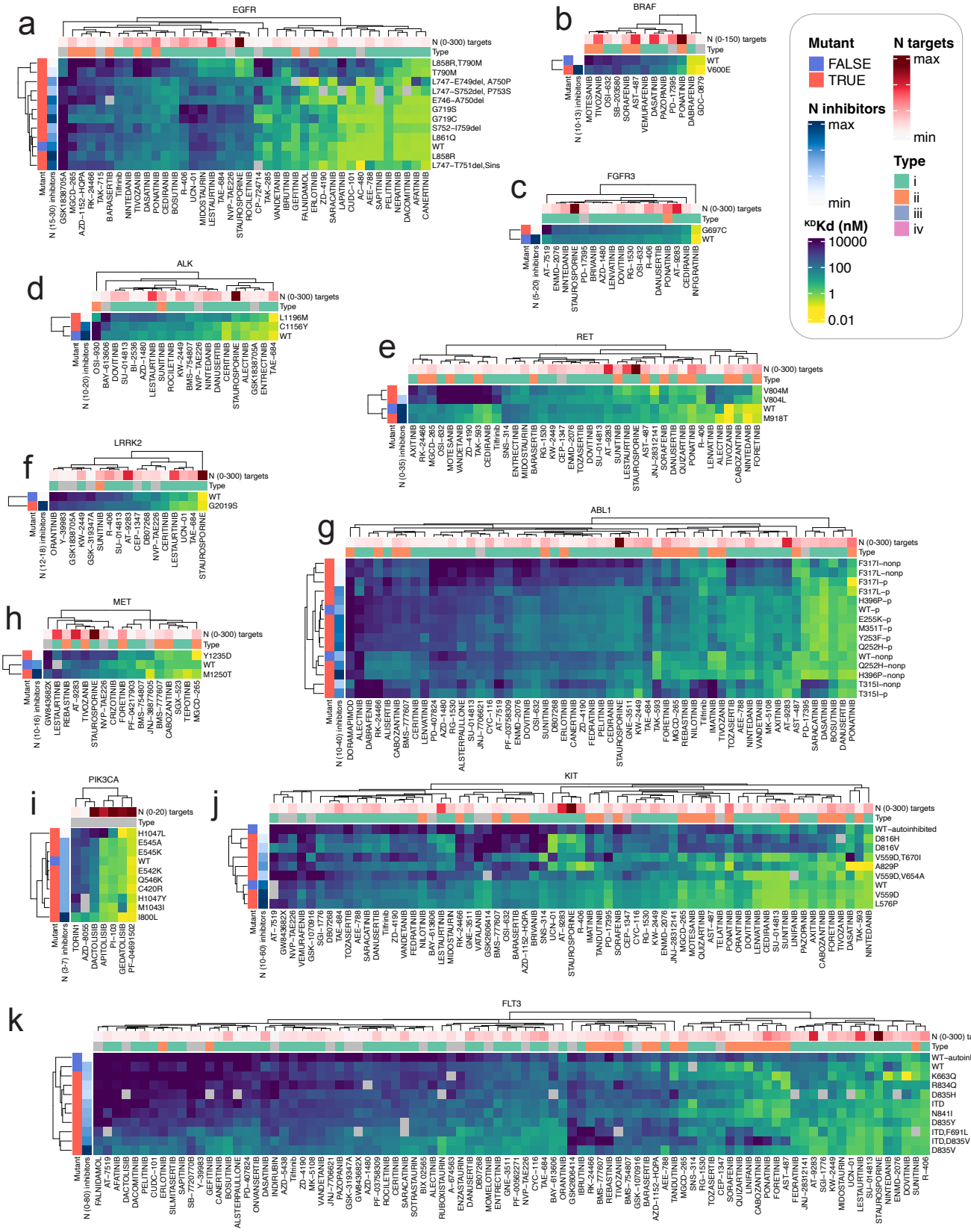

Supplementary Figure 3: **(a)** Heatmap with hierarchical clustering showing ^{KS}Kd values for OKL inhibitors against all variants of EGFR, **(b)** BRAF, **(c)** FGFR3, **(d)** ALK, **(e)** RET, **(f)** LRRK2, **(g)** ABL, **(h)** MET, **(i)** PIK3CA, **(j)** KIT, and **(k)** FLT3 that were assayed.

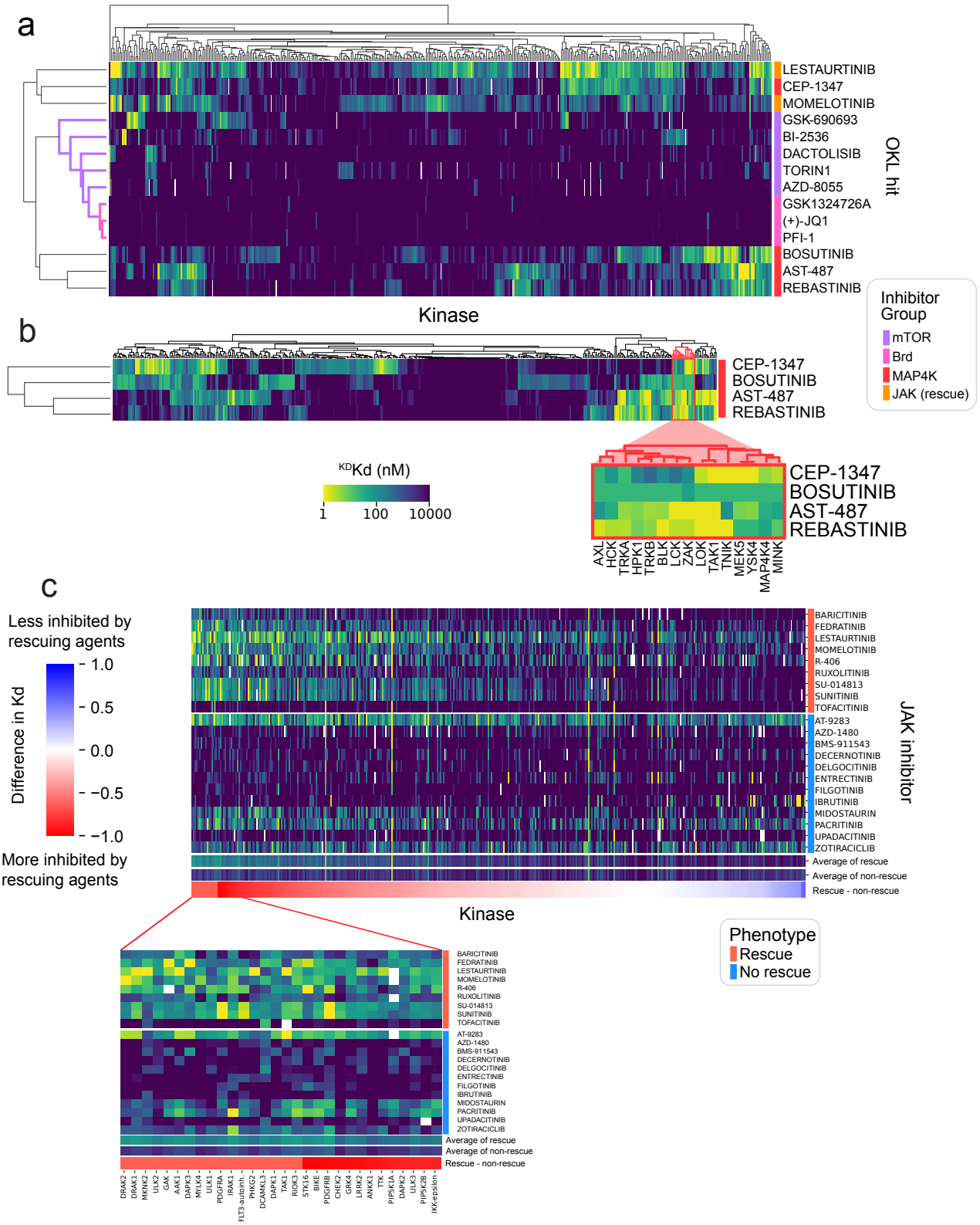

Supplementary Figure 4: **(a)** Clustermap of ^{KS}Kd values for OKL compounds that protect ReN VM cells from polyIC. The colored bars represent groupings by targets inhibited. **(b)** Clustermap of ^{KS}Kd values for the subset of OKL inhibitors denoted with a red bar in **(a)**, and a magnified view of the targets most potently inhibited by those hits. **(c)** Heatmap of ^{KS}Kd values for nominal JAK family inhibitors. Rows are sorted by phenotype; columns are sorted by the difference in ^{KS}Kd values between the rescuing and non-rescuing agents. A magnified view of the kinases that are preferentially inhibited by the rescuing agents is provided.

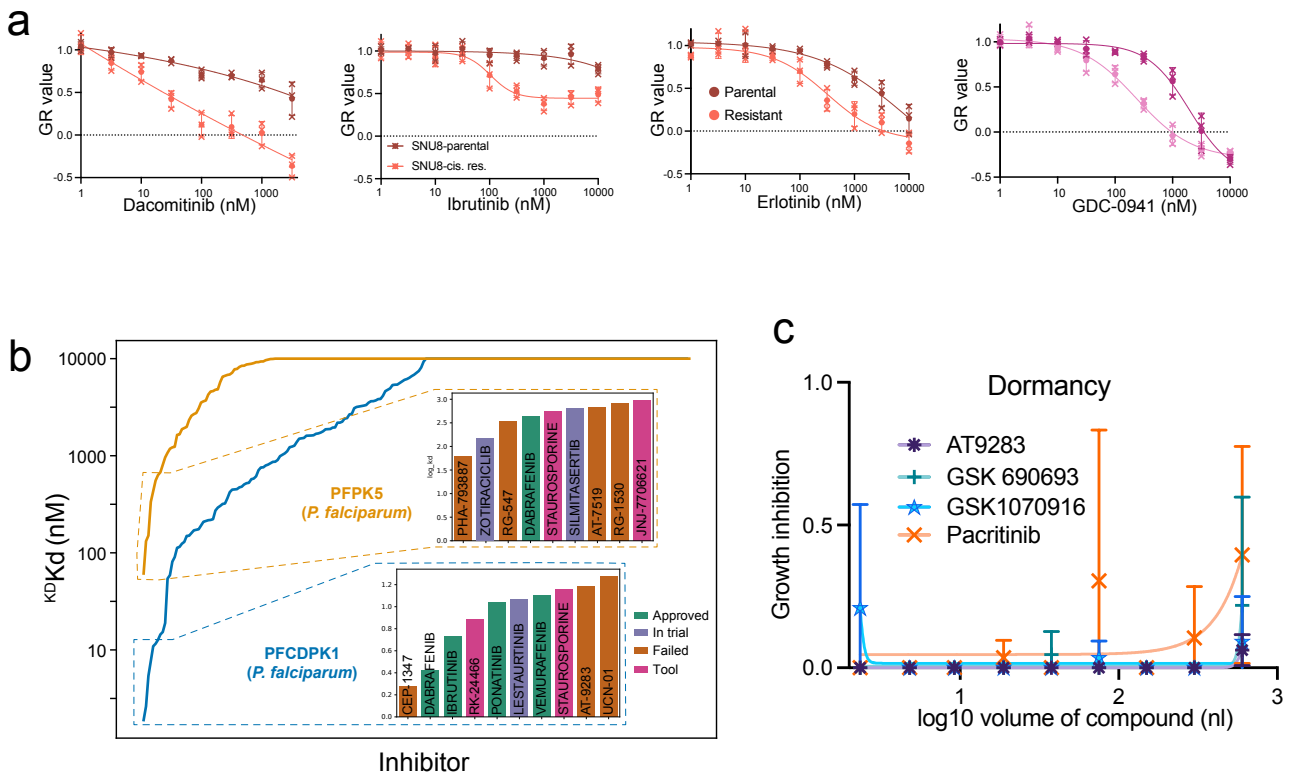

Supplementary Figure 5: **(a)** Dose response curves for the inhibitors shown in parental and cisplatin-resistant SNU8 cells after six-day treatments. **(b)** ^{KS}Kd values for OKL compounds against the *P. falciparum* (malaria) kinases, PFPK5 (orange) and PFCDPK1 (blue), the strongest inhibitors of each are shown in the inset bar graphs. **(c)** Dose-dependent growth inhibition of Mtb treated with the indicated drugs in the dormancy growth condition.

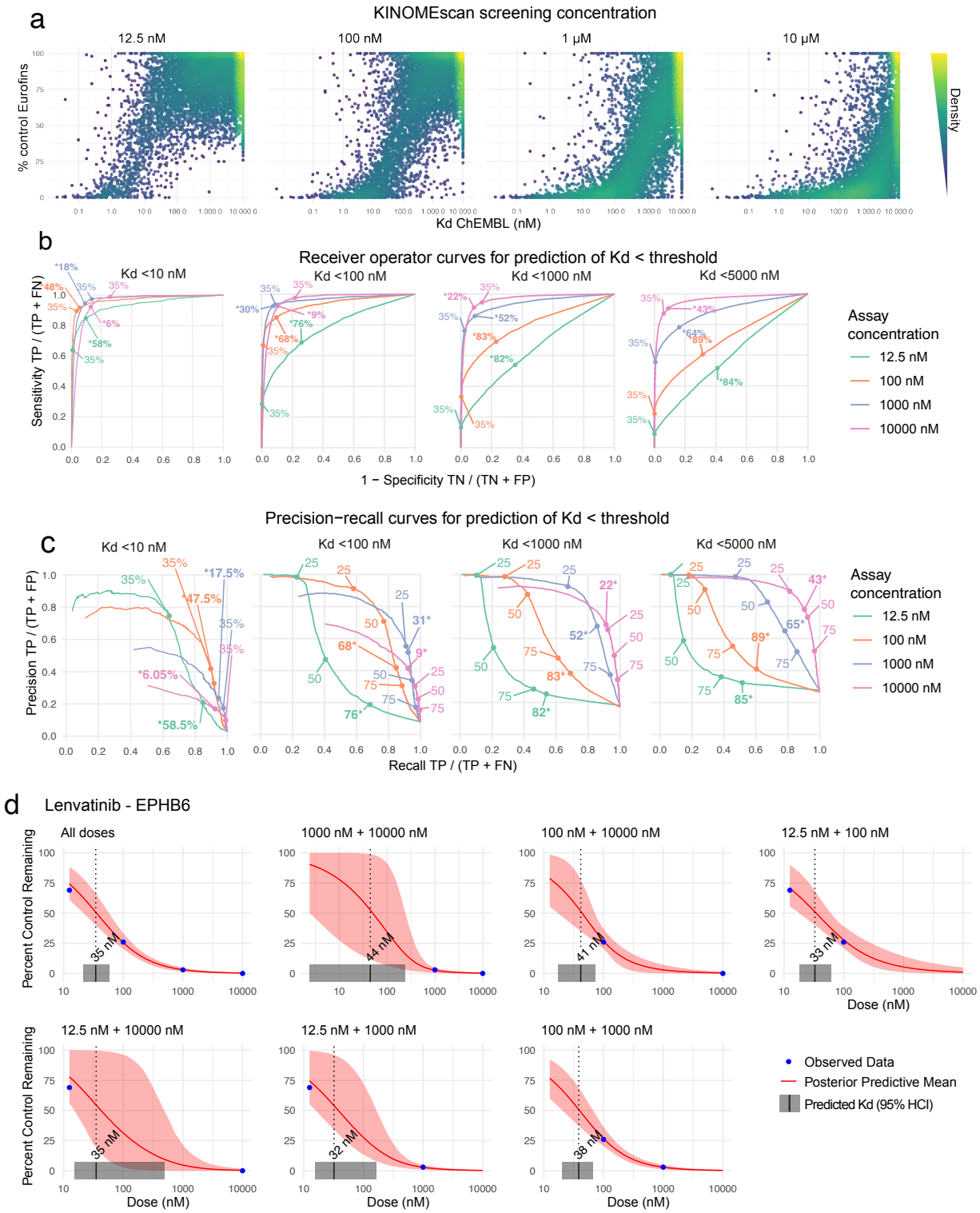

Supplementary Figure 6: (a) Scatterplots showing % control values for the screening concentrations indicated with respect to Kd data in ChEMBL. **(b)** False positive and negative rates for all percent control thresholds are plotted (taking ChEMBL data as the ground truth) on receiver operator curves, and the % control corresponding to the point closest to the upper left corner of the plot is identified as the optimal threshold. The optimal % control thresholds (denoted by * and bold font) and 35% are shown for each curve. **(c)** Precision-recall curves for predicting the Kd values shown using screening data collected at each assay concentration. The optimal % control thresholds (denoted by * and bold font) and 35% are shown for each curve. **(d)** Dose-response fits from the Bayesian model for lenvatinib binding EPHB6 across all four doses (first plot) and all two dose combinations. The credible 95% interval for the fit is shaded in red and for the ^{KS}Kd estimate in grey on the x-axis.

REFERENCES

1. Moret, N. *et al.* A resource for exploring the understudied human kinome for research and therapeutic opportunities. 2020.04.02.022277 Preprint at https://doi.org/10.1101/2020.04.02.022277 (2021).
2. Inhibitors Approved for Clinical Use | MRC PPU. https://www.ppu.mrc.ac.uk/list-clinically-approved-kinase-inhibitors.
3. Carles, F., Bourg, S., Meyer, C. & Bonnet, P. PKIDB: A Curated, Annotated and Updated Database of Protein Kinase Inhibitors in Clinical Trials. *Molecules* **23**, 908 (2018).
4. Bournez, C. *et al.* Comparative Assessment of Protein Kinase Inhibitors in Public Databases and in PKIDB. *Molecules* **25**, 3226 (2020).
5. Mullard, A. FDA approves 100th small-molecule kinase inhibitor. *Nature Reviews Drug Discovery* **24**, 891–895 (2025).
6. Klaeger, S. *et al.* The target landscape of clinical kinase drugs. *Science* **358**, (2017).
7. Davis, M. I. *et al.* Comprehensive analysis of kinase inhibitor selectivity. *Nat Biotechnol* **29**, 1046–1051 (2011).
8. Anastassiadis, T., Deacon, S. W., Devarajan, K., Ma, H. & Peterson, J. R. Comprehensive assay of kinase catalytic activity reveals features of kinase inhibitor selectivity. *Nat Biotechnol* **29**, 1039–1045 (2011).
9. Elkins, J. M. *et al.* Comprehensive characterization of the Published Kinase Inhibitor Set. *Nat Biotechnol* **34**, 95–103 (2016).
10. Reinecke, M. *et al.* Chemical proteomics reveals the target landscape of 1,000 kinase inhibitors. *Nat Chem Biol* 1–9 (2023) doi:10.1038/s41589-023-01459-3.
11. Zdrazil, B. *et al.* The ChEMBL Database in 2023: a drug discovery platform spanning multiple bioactivity data types and time periods. *Nucleic Acids Research* **52**, D1180–D1192 (2024).
12. Nguyen, D.-T. *et al.* Pharos: Collating protein information to shed light on the druggable genome. *Nucleic Acids Research* **45**, D995–D1002 (2017).
13. Gilson, M. K. *et al.* BindingDB in 2015: A public database for medicinal chemistry, computational chemistry and systems pharmacology. *Nucleic Acids Research* **44**, D1045–D1053 (2016).
14. Moret, N. *et al.* Cheminformatics Tools for Analyzing and Designing Optimized Small-Molecule Collections and Libraries. *Cell Chemical Biology* **26**, 765-777.e3 (2019).
15. Fabian, M. A. *et al.* A small molecule–kinase interaction map for clinical kinase inhibitors. *Nat Biotechnol* **23**, 329–336 (2005).
16. Drewry, D. H. *et al.* Progress towards a public chemogenomic set for protein kinases and a call for contributions. *PLOS ONE* **12**, e0181585 (2017).
17. Wells, C. I. *et al.* The Kinase Chemogenomic Set (KCGS): An Open Science Resource for Kinase Vulnerability Identification. *Int J Mol Sci* **22**, E566 (2021).
18. Karaman, M. W. *et al.* A quantitative analysis of kinase inhibitor selectivity. *Nat Biotechnol* **26**, 127–132 (2008).
19. Lahiry, P., Torkamani, A., Schork, N. J. & Hegele, R. A. Kinase mutations in human disease: interpreting genotype–phenotype relationships. *Nat Rev Genet* **11**, 60–74 (2010).
20. Bikker, J. A., Brooijmans, N., Wissner, A. & Mansour, T. S. Kinase Domain Mutations in Cancer: Implications for Small Molecule Drug Design Strategies. *J. Med. Chem.* **52**, 1493–1509 (2009).
21. Cheng, A. C., Eksterowicz, J., Geuns-Meyer, S. & Sun, Y. Analysis of kinase inhibitor selectivity using a thermodynamics-based partition index. *J Med Chem* **53**, 4502–4510 (2010).

22. Bosc, N., Meyer, C. & Bonnet, P. The use of novel selectivity metrics in kinase research. *BMC Bioinformatics* **18**, 17 (2017).
23. Essegian, D., Khurana, R., Stathias, V. & Schürer, S. C. The Clinical Kinase Index: A Method to Prioritize Understudied Kinases as Drug Targets for the Treatment of Cancer. *Cell Rep Med* **1**, 100128 (2020).
24. Raschi, E., Vasina, V., Poluzzi, E. & De Ponti, F. The hERG K+ channel: target and antitarget strategies in drug development. *Pharmacol Res* **57**, 181–195 (2008).
25. Dar, A. C., Das, T. K., Shokat, K. M. & Cagan, R. L. Chemical genetic discovery of targets and anti-targets for cancer polypharmacology. *Nature* **486**, 80–84 (2012).
26. Yang, X. *et al.* Kinase Inhibition-Related Adverse Events Predicted from in vitro Kinome and Clinical Trial Data. *J Biomed Inform* **43**, 376–384 (2010).
27. Burwinkel, B., Shiomi, S., Al Zaben, A. & Kilimann, M. W. Liver glycogenosis due to phosphorylase kinase deficiency: PHKG2 gene structure and mutations associated with cirrhosis. *Hum Mol Genet* **7**, 149–154 (1998).
28. Amemiya, T. *et al.* Elucidation of the molecular mechanisms underlying adverse reactions associated with a kinase inhibitor using systems toxicology. *NPJ Syst Biol Appl* **1**, 15005 (2015).
29. Alectinib. in *LiverTox: Clinical and Research Information on Drug-Induced Liver Injury* (National Institute of Diabetes and Digestive and Kidney Diseases, Bethesda (MD), 2012).
30. Dark Kinase Knowledgebase: an online compendium of knowledge and experimental results of understudied kinases | Nucleic Acids Research | Oxford Academic. https://academic.oup.com/nar/article/49/D1/D529/5932842?login=false.
31. Sharma, K. R., Colvis, C. M., Rodgers, G. P. & Sheeley, D. M. Illuminating the druggable genome: Pathways to progress. *Drug Discov Today* **29**, 103805 (2024).
32. Vijayan, R. S. K. *et al.* Conformational Analysis of the DFG-Out Kinase Motif and Biochemical Profiling of Structurally Validated Type II Inhibitors. *J. Med. Chem.* **58**, 466–479 (2015).
33. Zhang, J., Yang, P. L. & Gray, N. S. Targeting cancer with small molecule kinase inhibitors. *Nat Rev Cancer* **9**, 28–39 (2009).
34. Berman, H. M. *et al.* The Protein Data Bank. *Nucleic Acids Res* **28**, 235–242 (2000).
35. Hanson, S. M. *et al.* What makes a kinase promiscuous for inhibitors? *Cell Chem Biol* **26**, 390-399.e5 (2019).
36. Manning, G., Whyte, D. B., Martinez, R., Hunter, T. & Sudarsanam, S. The Protein Kinase Complement of the Human Genome. *Science* **298**, 1912–1934 (2002).
37. Wang, X., Ding, J. & Meng, L. PI3K isoform-selective inhibitors: next-generation targeted cancer therapies. *Acta Pharmacol Sin* **36**, 1170–1176 (2015).
38. Lindberg, M. F. & Meijer, L. Dual-Specificity, Tyrosine Phosphorylation-Regulated Kinases (DYRKs) and cdc2-Like Kinases (CLKs) in Human Disease, an Overview. *Int J Mol Sci* **22**, 6047 (2021).
39. Song, M. *et al.* Cdc2-like kinases: structure, biological function, and therapeutic targets for diseases. *Sig Transduct Target Ther* **8**, 1–25 (2023).
40. Schröder, M. *et al.* DFG-1 Residue Controls Inhibitor Binding Mode and Affinity, Providing a Basis for Rational Design of Kinase Inhibitor Selectivity. *J. Med. Chem.* **63**, 10224–10234 (2020).
41. Rodriguez, S. *et al.* Genome-encoded cytoplasmic double-stranded RNAs, found in C9ORF72 ALS-FTD brain, propagate neuronal loss. *Sci Transl Med* **13**, eaaz4699 (2021).
42. Konig, L.E. *et al.* TYK2 as a novel therapeutic target in Alzheimer's Disease with TDP-43 inclusions. *Nature Neuroscience* (Under review.).
43. Wong, P.-M., Puente, C., Ganley, I. G. & Jiang, X. The ULK1 complex. *Autophagy* **9**, 124–137 (2013).

44. Levin-Salomon, V., Bialik, S. & Kimchi, A. DAP-kinase and autophagy. *Apoptosis* **19**, 346–356 (2014).
45. Selvaraj, V. *et al.* Baricitinib in hospitalised patients with COVID-19: A meta-analysis of randomised controlled trials. *eClinicalMedicine* **49**, (2022).
46. Zhang, Z., Yang, X., Song, Y.-Q. & Tu, J. Autophagy in Alzheimer's disease pathogenesis: Therapeutic potential and future perspectives. *Ageing Research Reviews* **72**, 101464 (2021).
47. Jung, C. H., Ro, S.-H., Cao, J., Otto, N. M. & Kim, D.-H. mTOR regulation of autophagy. *FEBS Lett* **584**, 1287–1295 (2010).
48. Sakamaki, J. *et al.* Bromodomain Protein BRD4 Is a Transcriptional Repressor of Autophagy and Lysosomal Function. *Mol Cell* **66**, 517-532.e9 (2017).
49. Petrova, V. *et al.* Multi-Kinase Inhibition of STE20 Kinases is Neuroprotective Against Chemotherapy-Induced Axon Degeneration. SSRN Scholarly Paper at https://doi.org/10.2139/ssrn.5380584 (2025).
50. Bos, P. H. *et al.* Development of MAP4 Kinase Inhibitors as Motor Neuron-Protecting Agents. *Cell Chem Biol* **26**, 1703-1715.e37 (2019).
51. Davis, A., Tinker, A. V. & Friedlander, M. 'Platinum resistant' ovarian cancer: what is it, who to treat and how to measure benefit? *Gynecol Oncol* **133**, 624–631 (2014).
52. Granados, M. L., Hudson, L. G. & Samudio-Ruiz, S. L. Contributions of the Epidermal Growth Factor Receptor to Acquisition of Platinum Resistance in Ovarian Cancer Cells. *PLoS One* **10**, e0136893 (2015).
53. Zhao, J. *et al.* FGFR3 phosphorylates EGFR to promote cisplatin-resistance in ovarian cancer. *Biochemical Pharmacology* **190**, 114536 (2021).
54. Wilken, J. A. *et al.* EGFR/HER-targeted therapeutics in ovarian cancer. *Future Med Chem* **4**, 447–469 (2012).
55. Zeng, J. *et al.* Protein kinases PknA and PknB independently and coordinately regulate essential Mycobacterium tuberculosis physiologies and antimicrobial susceptibility. *PLOS Pathogens* **16**, e1008452 (2020).
56. Thongdee, P. *et al.* Virtual Screening Identifies Novel and Potent Inhibitors of Mycobacterium tuberculosis PknB with Antibacterial Activity. *J. Chem. Inf. Model.* **62**, 6508–6518 (2022).
57. Xu, J. *et al.* A novel protein kinase inhibitor IMB-YH-8 with anti-tuberculosis activity. *Sci Rep* **7**, 5093 (2017).
58. Larkins-Ford, J. *et al.* Systematic measurement of combination-drug landscapes to predict *in vivo* treatment outcomes for tuberculosis. *Cell Systems* **12**, 1046-1063.e7 (2021).
59. Singer, J. W. *et al.* Comprehensive kinase profile of pacritinib, a nonmyelosuppressive Janus kinase 2 inhibitor. *J Exp Pharmacol* **8**, 11–19 (2016).
60. Keenan, S. M. & Welsh, W. J. Characteristics of the Plasmodium falciparum PK5 ATP-binding site: implications for the design of novel antimalarial agents. *J Mol Graph Model* **22**, 241–247 (2004).
61. Ou, S.-H. I., Bartlett, C. H., Mino-Kenudson, M., Cui, J. & Iafrate, A. J. Crizotinib for the Treatment of ALK-Rearranged Non-Small Cell Lung Cancer: A Success Story to Usher in the Second Decade of Molecular Targeted Therapy in Oncology. *Oncologist* **17**, 1351–1375 (2012).
62. Shaw, A. T. *et al.* Crizotinib in ROS1-rearranged advanced non-small-cell lung cancer (NSCLC): updated results, including overall survival, from PROFILE 1001. *Ann Oncol* **30**, 1121–1126 (2019).
63. Hafner, M. *et al.* Multiomics Profiling Establishes the Polypharmacology of FDA-Approved CDK4/6 Inhibitors and the Potential for Differential Clinical Activity. *Cell Chem Biol* **26**, 1067-1080.e8 (2019).
64. Dar, A. C., Das, T. K., Shokat, K. M. & Cagan, R. L. Chemical genetic discovery of targets and anti-targets for cancer polypharmacology. *Nature* **486**, 80–84 (2012).

65. Zhao, L., Zhao, J., Zhong, K., Tong, A. & Jia, D. Targeted protein degradation: mechanisms, strategies and application. *Sig Transduct Target Ther* **7**, 113 (2022).
66. Wodicka, L. M. *et al.* Activation State-Dependent Binding of Small Molecule Kinase Inhibitors: Structural Insights from Biochemistry. *Chemistry & Biology* **17**, 1241–1249 (2010).
67. Abril-Pla, O. *et al.* PyMC: a modern, and comprehensive probabilistic programming framework in Python. *PeerJ Comput. Sci.* **9**, e1516 (2023).
68. Masters, J. R. *et al.* Short tandem repeat profiling provides an international reference standard for human cell lines. *Proceedings of the National Academy of Sciences* **98**, 8012–8017 (2001).
69. Mills, C. E. *et al.* Multiplexed and reproducible high content screening of live and fixed cells using Dye Drop. *Nat Commun* **13**, 6918 (2022).
70. Hafner, M., Niepel, M., Chung, M. & Sorger, P. K. Growth rate inhibition metrics correct for confounders in measuring sensitivity to cancer drugs. *Nature methods* **13**, 521–7 (2016).
71. Abraham, M. J. *et al.* GROMACS: High performance molecular simulations through multi-level parallelism from laptops to supercomputers. *SoftwareX* **1–2**, 19–25 (2015).
72. Gromacs: A parallel computer for molecular dynamics simulations – ScienceOpen. https://www.scienceopen.com/book?vid=59290415-039c-4900-8e95-d649687a2473.
73. Guvench, O. *et al.* CHARMM Additive All-Atom Force Field for Carbohydrate Derivatives and Its Utility in Polysaccharide and Carbohydrate–Protein Modeling. *J. Chem. Theory Comput.* **7**, 3162–3180 (2011).
74. Malde, A. K. *et al.* An Automated Force Field Topology Builder (ATB) and Repository: Version 1.0. *J. Chem. Theory Comput.* **7**, 4026–4037 (2011).
75. Haug, E. J., Arora, J. S. & Matsui, K. A steepest-descent method for optimization of mechanical systems. *J Optim Theory Appl* **19**, 401–424 (1976).
76. Parrinello, M. & Rahman, A. Polymorphic transitions in single crystals: A new molecular dynamics method. *Journal of Applied Physics* **52**, 7182–7190 (1981).
77. Gunsteren, W. F. V. & Berendsen, H. J. C. A Leap-frog Algorithm for Stochastic Dynamics. *Molecular Simulation* https://doi.org/10.1080/08927028808080941 (1988) doi:10.1080/08927028808080941.
78. Darden, T., York, D. & Pedersen, L. Particle mesh Ewald: An N·log(N) method for Ewald sums in large systems. *The Journal of Chemical Physics* **98**, 10089–10092 (1993).